

A Modular Control Architecture for Airborne Wind Energy Systems

Rapp, Sebastian; Schmehl, Roland; Oland, Espen; Schmidt, Sture; Haas, Thomas; Meyers, Johan

DOI

[10.2514/6.2019-1419](https://doi.org/10.2514/6.2019-1419)

Publication date

2019

Document Version

Final published version

Published in

AIAA Scitech 2019 Forum

Citation (APA)

Rapp, S., Schmehl, R., Oland, E., Schmidt, S., Haas, T., & Meyers, J. (2019). A Modular Control Architecture for Airborne Wind Energy Systems. In *AIAA Scitech 2019 Forum: 7-11 January 2019, San Diego, California, USA* Article AIAA 2019-1419 American Institute of Aeronautics and Astronautics Inc. (AIAA). <https://doi.org/10.2514/6.2019-1419>

Important note

To cite this publication, please use the final published version (if applicable).
Please check the document version above.

Copyright

Other than for strictly personal use, it is not permitted to download, forward or distribute the text or part of it, without the consent of the author(s) and/or copyright holder(s), unless the work is under an open content license such as Creative Commons.

Takedown policy

Please contact us and provide details if you believe this document breaches copyrights.
We will remove access to the work immediately and investigate your claim.

Green Open Access added to TU Delft Institutional Repository

'You share, we take care!' – Taverne project

<https://www.openaccess.nl/en/you-share-we-take-care>

Otherwise as indicated in the copyright section: the publisher is the copyright holder of this work and the author uses the Dutch legislation to make this work public.



A Modular Control Architecture for Airborne Wind Energy Systems

Sebastian Rapp* and Roland Schmehl†
Delft University of Technology, Faculty of Aerospace Engineering

Espen Oland‡ and Sture Smidt§
Kitemill AS

Thomas Haas¶ and Johan Meyers||
KU Leuven, Department of Mechanical Engineering

Airborne wind energy is an emerging technology that uses tethered unmanned aerial vehicles for harvesting wind energy at altitudes higher than conventional towered wind turbines. To make the technology competitive to other renewable energy technologies an automatic control system is required that allows autonomously operating the system throughout all phases of flight. In this study a modular control system is presented, adapting the underlying kinematic and dynamic framework from conventional aerospace terminology and applying this to tethered crosswind flight with varying tether length. The high level control strategy in form of a state machine as well as the cascaded flight control structure consisting of path-following guidance and control, attitude and rate loop is presented along with the winch controller. The present work is a first step towards a methodology for the systematic development of reliable and high-performance control solutions for airborne wind energy systems. Models for the airborne system, ground station, as well as the tether connecting the ground system with the airframe will be presented. Results from a simulation study in a realistic wind field will be used to demonstrate the feasibility of the proposed concept and to identify particularly challenging situations in the operational envelope.

I. Introduction

AIRBORNE WIND ENERGY (AWE) is an emerging branch within the sustainable energy systems portfolio that aims to exploit wind energy resources at altitudes higher than conventional towered wind turbines by means of kites and tethered aircraft. In general, AWE systems can be subdivided into two main categories. On the one hand, drag-based AWE systems fly crosswind patterns with constant tether length while the kinetic energy of the relative flow is converted into electrical power using on-board generators. The electricity is transmitted via a conductive tether to the ground. On the other hand, AWE systems with a ground-based generator operate in a so called *pumping-cycle mode* and use the aerodynamic force of the kite or aircraft to uncoil the tether from a drum, which turns a generator that converts the mechanical into electrical power on the ground. When the maximum tether length is reached, the aircraft will fly back towards the ground station, while the tether is reeled in. Since the generator acts as a motor during the retraction phase a fraction of the produced power is consumed. Once the minimum tether length is reached, the cycle starts all over again [1, 2]. For a more detailed overview of the different concepts it is referred to [3]. In the present work the focus lies on the controller development for AWE systems operated in pumping cycle mode.

Historically, most of the stakeholders in this field started to study the potential of flexible kite power systems, which is also reflected by the fact that most of the published papers are dedicated to the design of control systems applicable to flexible wing kite power systems [4–8]. However, due to better scalability and efficiency the trend goes towards

*PhD Researcher, Delft University of Technology, Kluyverweg 1, 2629HS, Delft, The Netherlands, s.rapp@tudelft.nl.

†Associate Professor, Delft University of Technology, Kluyverweg 1, 2629HS, Delft, The Netherlands, r.schmehl@tudelft.nl.

‡Control System Manager, Kitemill AS, Miltzowsgate 2, 5700 Voss, Norway, eo@kitemill.no

§Head of Kite Discipline, Kitemill AS, Miltzowsgate 2, 5700 Voss, Norway, ss@kitemill.no

¶PhD Researcher, KU Leuven, Celestijnenlaan 300, 3001 Leuven, Belgium, thomas.haas@kuleuven.be

||Associate Professor, KU Leuven, Celestijnenlaan 300, 3001 Leuven, Belgium, johan.meyers@kuleuven.be

rigid wing AWE systems reflected by the fact that almost all companies in the field operate rigid-wing prototypes. Nevertheless, available publications on rigid wing kite control are rare. Although the reliability of the control system plays a paramount role that decides upon the success of this new technology most of the available literature focuses on flight path optimization instead of the development of more robust control solutions. One recent control approach that is not dedicated to flight path optimization is presented in [9]. In the paper, the authors focus on take-off and landing control, including a transition to a loiter-like figure of eight pattern flight on a constant tether length using linear controllers.

To the best authors knowledge no modular control architecture for the full operational envelope for rigid wing AWE systems has been published yet. The present work tries to fill this gap where a modular control architecture similar to the one presented in [9], but eventually applicable to the whole range of operational modes including take-off, transition, pumping cycle mode and landing is presented. Moreover, instead of using linear control techniques a model-based nonlinear flight controller is developed that eventually increases the operational envelope and the performance of the AWE system in situations where linear control techniques might fail. In the future, the presented control approach could be augmented with adaptive control techniques to increase the robustness towards failures or unforeseen environmental conditions. The modularity of the control architecture aims to achieve a high degree of reusability especially of the outer-loop module, such that it can be implemented conveniently on different platforms. The guidance module will build up on a previous publication by the second author [8]. The proposed control approach aims at providing control modules with defined interfaces that allow to exchange and modify different parts of the overall controller conveniently. This enables operators with existing prototypes to only use specific modules without the need to re-implement the entire control system. Especially the guidance module might be of interest for AWE companies, since it is entirely model independent, and applicable to kites operated in pumping or drag mode alike. Furthermore, applying systematically the concept of pseudo control hedging [10] a flight envelope protection system is implemented ensuring that no unfeasible commands are passed to the next loop. Constraining states is of particular importance in this application since the aircraft is usually operated at near stall conditions while following a three dimensional curved path which requires to constrain commands from the outer loops in a systematic manner. Such an envelope protection for airborne wind energy systems has not been presented yet apart from model predictive control approaches where constraints are directly embedded in the optimal control problem formulation [11].

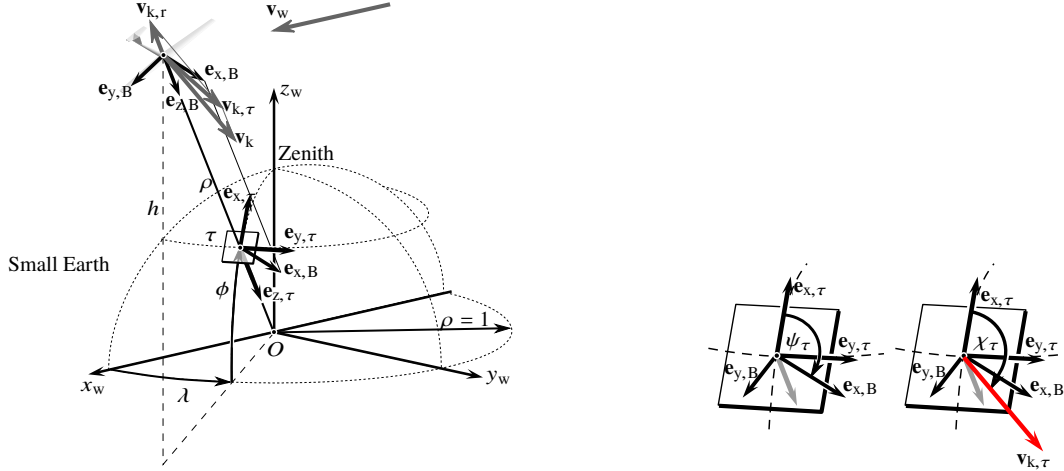
The performance of the control system is demonstrated by means of a simulation study. To create a realistic simulation framework a detailed aerodynamic analysis using computational fluid dynamics and *XFLR5* calculations of the 5 kW prototype of *Kitemill AS* have been carried out. The robustness of the control system towards wind gusts and atmospheric turbulence is assessed using three-dimensional transient wind field data generated by large-eddy simulations (LES) of a pressure-driven boundary layer.

The paper is structured as follows. In section II the simulation models for aircraft, tether, ground station as well as the wind field are presented. In section III a detailed derivation of the different controllers is presented. Simulation results are presented in section IV followed by a conclusion in section V.

II. Reference Frames and Simulation Models

A. Reference Frames

Fig. 1a displays the wind frame W where the x_W axis is pointing in downwind direction and the z_W axis is the local surface normal vector, while the y_W forms a right-hand coordinate system together with x_W and z_W . The origin of the W frame is at the ground station. Note, this definition of the wind frame differs from the conventional definition found in the aerospace literature where the wind frame is a local body fixed frame [12, p. 76]. Furthermore, Fig. 1a displays the tangential plane frame τ which will be used as a reference frame for the guidance loop. The z_τ axis is pointing towards the origin of the wind frame W , the x_τ axis points towards the zenith position, which is located above the ground station. Note that the τ -frame is defined equivalently to the North-East-Down frame (O) (cf. [13, p. 12]) for a small earth with radius one and center at the origin of the W frame. The position of the aircraft with respect to the W frame will be either given in Cartesian coordinates x_W , y_W and z_W or in spherical coordinates using the longitude λ and latitude ϕ as well as the Euclidean distance of the aircraft to the origin of W . The body-fixed frame B [14, p. 57], the kinematic frame K [14, p. 58] as well as the aerodynamic frame A [14, p. 61] are defined according to aerospace convention.



(a) Visualization of wind frame W , body-fixed frame B and (b) Definition of the tangential plane heading Ψ_τ and tangential plane course χ_τ .

Fig. 1 Reference frames

B. Tethered Aircraft Model

The aircraft is modeled as a standard six degrees of freedom rigid body with an additional term in the translational equations of motion representing the tether force. No additional term in the rotational dynamics appears since it is assumed that the tether is attached to the center of gravity of the aircraft. A detailed derivation of the governing equations of motion can be found for instance in [12]. The translational dynamics are defined as

$$\begin{pmatrix} \dot{u}_k \\ \dot{v}_k \\ \dot{w}_k \end{pmatrix}_B = -(\boldsymbol{\omega}^{OB})_B \times (\mathbf{v}_k)_B + \frac{1}{m_k} ((\mathbf{F}_a)_B + (\mathbf{F}_g)_B + (\mathbf{F}_t)_B) \quad (1)$$

where $(\mathbf{v}_k)_B \in \mathbb{R}^{3 \times 1}$ is the kinematic aircraft velocity in the B frame with components u_k, v_k and w_k , m_k is the mass of the aircraft, $(\boldsymbol{\omega}^{OB})_B \in \mathbb{R}^{3 \times 1}$ is the angular velocity vector between the B and O frame containing the roll rate p , pitch rate q as well as yaw rate r , $(\mathbf{F}_a)_B \in \mathbb{R}^{3 \times 1}$ is the aerodynamic force, $(\mathbf{F}_g)_B \in \mathbb{R}^{3 \times 1}$ is the gravity force and $(\mathbf{F}_t)_B \in \mathbb{R}^{3 \times 1}$ is the tether force. The rotational dynamics are defined as

$$(\dot{\boldsymbol{\omega}}^{OB})_B = \begin{pmatrix} \dot{p} \\ \dot{q} \\ \dot{r} \end{pmatrix}_B = \mathbf{J}^{-1} (-(\boldsymbol{\omega}^{OB})_B \times \mathbf{J} (\boldsymbol{\omega}^{OB})_B + (\mathbf{M}_a)_B) \quad (2)$$

where $\mathbf{J} \in \mathbb{R}^{3 \times 3}$ is the inertia tensor, and $(\mathbf{M}_a)_B \in \mathbb{R}^{3 \times 1}$ is the resulting aerodynamic moment around the center of gravity of the aircraft. The attitude is parameterized using quaternions, hence the equation for the attitude propagation is given by

$$\dot{\mathbf{q}} = \begin{pmatrix} \dot{q}_1 \\ \dot{q}_2 \\ \dot{q}_3 \\ \dot{q}_4 \end{pmatrix} = \begin{pmatrix} -q_2 & -q_3 & -q_4 & q_1 \\ q_1 & -q_4 & q_3 & q_2 \\ q_4 & q_1 & -q_2 & q_3 \\ -q_3 & q_2 & q_1 & q_4 \end{pmatrix} \begin{pmatrix} p \\ q \\ r \\ 2k\kappa \end{pmatrix} \quad (3)$$

The quaternion attitude propagation equation Eq. (3) is implemented with gradient feedback as described in [15] with $\kappa = 1 - q_1^2 - q_2^2 - q_3^2 - q_4^2$ otherwise numerical inaccuracies can lead to a violation of the unity norm condition of the

quaternion vector. The position of the aircraft's center of gravity $(\mathbf{p}^G)_O$ in the O frame will be propagated according to

$$(\mathbf{p}^G)_O = \begin{pmatrix} \dot{p}_x^G \\ \dot{p}_y^G \\ \dot{p}_z^G \end{pmatrix}_O = \begin{pmatrix} q_1^2 + q_2^2 - q_3^2 - q_4^2 & 2(q_2q_3 - q_1q_4) & 2(q_1q_3 + q_2q_4) \\ 2(q_2q_3 + q_1q_4) & q_1^2 - q_2^2 + q_3^2 - q_4^2 & 2(q_3q_4 - q_1q_2) \\ 2(q_2q_4 - q_1q_3) & 2(q_3q_4 + q_1q_2) & q_1^2 - q_2^2 - q_3^2 + q_4^2 \end{pmatrix} \begin{pmatrix} u_k \\ v_k \\ w_k \end{pmatrix}_B \quad (4)$$

The states of the tethered aircraft are the three kinematic velocity components in the bodyfixed frame u_k, v_k and w_k , the body rates p, q, r , the quaternions q_1, q_2, q_3 and q_4 , as well as the position in the O frame with components p_x^G, p_y^G and p_z^G . At the moment full state feedback is assumed, and the controller requires measurements for mean wind direction on the ground ξ , position, velocity, orientation, angle of attack α , sideslip angle β , airspeed V_a , rotational rates as well as the total tether force F_t measured on the ground and at the aircraft. The reason for measuring the tether force on the aircraft as well as on the ground is that due to the tether drag and weight the force measured on the ground differs from the tether force acting on the aircraft.

As a reference model, the geometric and aerodynamic characteristics of the small scale 5 kW prototype developed by *Kitemill AS* are used. The aerodynamic model contains the main dependencies of the force and moment coefficients on relevant aircraft states in form of multidimensional lookup tables.

C. Tether Model

The tether is modeled as a particle system where the individual particles are connected via spring-damper elements. For each particle the point mass dynamics are defined incorporating tether drag and tether weight. During reelout or reelin the unstretched length of each spring-damper as well as the mass of each particle is adapted proportionally to the current change in tether length. A detailed explanation of the implemented tether model can be found in a previous work of the second author [16].

D. Ground Station

In general, the ground station consists of the generator and the winch. In this work the only relevant component for the controller development is represented by the winch which can be modeled as a scalar first order system given by

$$\dot{\omega}_w = J_w^{-1} (-\kappa_w \omega_w + r_w F_t + M_c) \quad (5)$$

where ω_w represents the rotational speed of the winch, r_w is the radius of the winch, which is assumed to be constant despite the reeling in or out of the tether, $\kappa_w > \forall t$ is a viscous friction coefficient, F_t is the tether force and M_c is the motor/generator torque which represents the control input. The electrical drive of the ground station is not modeled in this work.

E. Wind Field Model

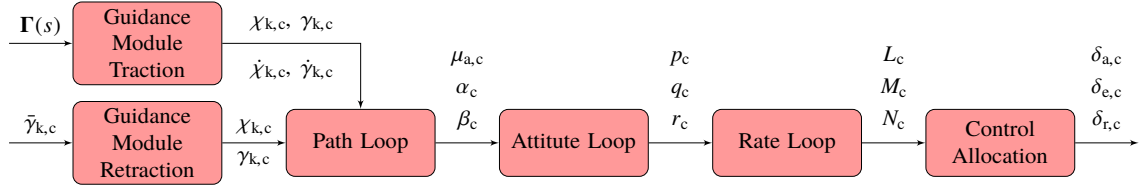
In order to test the controller in a realistic wind field, a four-dimensional velocity field is integrated into the simulation framework. The wind field data was generated by means of large-eddy simulations of a pressure-driven boundary layer. The computations were carried out using *SPWind*, a pseudo-spectral simulation code developed at KU Leuven. Information on the specification and the implementation of the flow solver can be found in [17–19]. The wind field data is available at a spatial resolution of approximately $20 \text{ m} \times 15 \text{ m} \times 7 \text{ m}$ in x_w, y_w and z_w direction, respectively, for a time series of several minutes and stored in form of lookup tables. During the simulation the wind velocity vector at the location of the aircraft is obtained through linear interpolation of the adjacent vertex velocity vectors.

III. Controller Development

A. Control Architecture and State Machine

The high level control architecture is displayed in Fig. 2. On the highest level the controller can be decomposed into the flight and the winch control system, represented by the upper and lower cascade in Fig. 2. The task of the flight control system is to control the tangential motion on the sphere while the radial direction is controlled by the winch. The blocks correspond to modules that will be discussed in more detail in the following sections. In general, each block has one input and one output signal corresponding to the set point that has to be tracked by the module as well as the

Flight Controller:



Winch Controller:

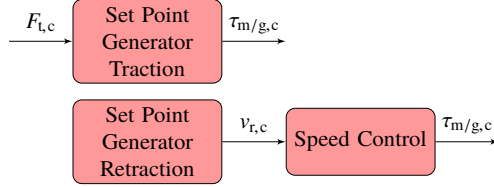


Fig. 2 Cascaded control structure of flight and winch control system for traction and retraction mode.

commanded set point for the next module. Blocks with two inputs are subdivided into two sub modules (not displayed), one module for the traction and one for the retraction phase. All remaining modules are the same for both traction and retraction, although different gains and filter bandwidths are used for increased performance. Based on the current state π_i , as defined in Table 1, the output from either the traction or retraction module is passed on to the next module. The flight control guidance module input of the traction phase is the path parameterization $\Gamma(s) \in \mathbb{R}^{3 \times 1}$ with $s \in (0, 2\pi)$. Within the module the required kinematic (subscript k) course $\chi_{k,c}$ and kinematic path angle $\gamma_{k,c}$ as well as the required course rate $\dot{\chi}_{k,c}$ and path angle rate $\dot{\gamma}_{k,c}$ are calculated based on the current position. The guidance module input of the retraction phase is the desired path angle $\tilde{\gamma}_{k,c}$ and the output signal is the kinematic course $\chi_{k,c}$ and kinematic path angle $\gamma_{k,c}$. Note, $\tilde{\gamma}_{k,c}$ and $\gamma_{k,c}$ differ from each other only in the final part of the retraction phase where the path angle $\tilde{\gamma}_{k,c}$ is linearly increased to a fixed value before the transition back into the traction phase is triggered. This maneuver is used to reduce the kinetic energy of the aircraft before the turn. The path loop will track the commands from the guidance module and calculates attitude commands for aerodynamic (subscript a) bank angle $\mu_{a,c}$ and angle of attack α_c . Note, α and β always refer to the aerodynamic and not kinematic angles if not indicated otherwise. The attitude loop tracks the attitude commands and transforms them into roll-, pitch-, and yaw rate commands p_c , q_c and r_c , respectively. Finally, the rate loop calculates the control moments which are then distributed among the actuators in the control allocation block, which results in an aileron command δ_a , elevator command δ_e and rudder command δ_r . The winch controller requires only a set point generator for traction and retraction phase as well as a speed controller. During the traction phase, a reference torque $\tau_{m/g,c}$ is directly calculated based on the tether force set point $F_{t,c}$. During the retraction phase a fixed reeling in speed $v_{r,c}$ is commanded that will be tracked by a speed controller, which outputs a corresponding torque command $\tau_{m/g,c}$. In both cases, the torque commands will be tracked by the electrical drive control system.

Fig. 3 shows the state-machine that is used to switch between the different control modules. The individual states are defined in Table 1. The modeled prototype of *Kitemill AS* allows vertical takeoff and landing (VTOL). A VTOL controller including the transition into pumping cycle mode is implemented in the simulation framework, however a detailed description of the VTOL controller is out of the scope of this paper and will be part of a future publication. Essentially, a similar control approach for the winch and the flight controller is adapted from [20], where a VTOL controller for a flexible kite system is presented. The interface to the pumping cycle mode is given by a transition into π_0 . In this work it will be assumed that the aircraft was guided in downwind direction to the operational altitude that fulfills the latitude condition $\phi > \phi_0 + \Delta\phi_0$, where the VTOL controller keeps the aircraft in a hover state (not displayed) until π_0 is triggered. ϕ_0 is the mean latitude angle of the path and $0^\circ \leq \Delta\phi_0 \leq 10^\circ$ is a small offset. The transition from the launching state to the crosswind flight state is initiated by fast reeling in of the tether. As soon as the airspeed exceeds the minimum airspeed, here denoted with $V_{a,min}$, the transition to π_1 is triggered. In this state the path-following controller is activated and the guidance law is initialized with a first guess of the closest point on the path relative to the current aircraft position. Flying towards the path decreases the elevation angle, which triggers the transition into the traction phase state π_2 if it reaches a value below $\phi_m + \Delta_t$ ($0^\circ \leq \Delta_t \leq 10^\circ$) and the winch starts reeling out the

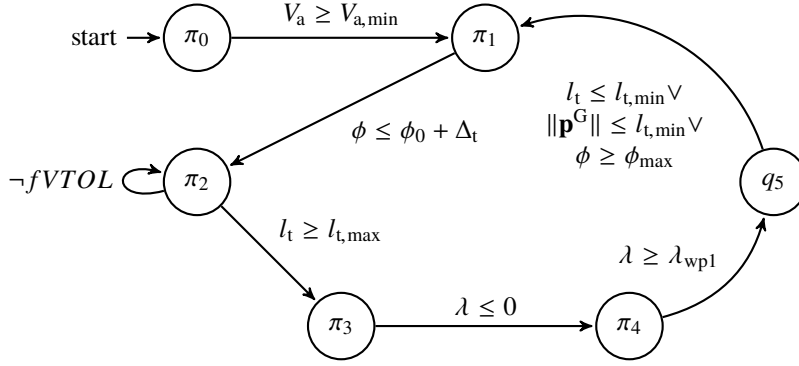


Fig. 3 State-machine for the pumping cycle mode.

tether. The intermediate state π_1 was added to start reeling out after the aircraft is sufficiently steered into the downwind direction. If the tether is reeled out immediately this could lead to a drop in tether tension during the initial turn. As long as no landing is issued by the supervisor layer ($fVTOL = 1$) the kite remains in state π_2 . The transition into π_3 is triggered as soon as the specified tether length is reached. This state can be interpreted as an intermediate state which is left as soon as the aircraft flies into the negative half plane of the wind window defined by a negative longitude angle $\lambda < 0$. This triggers the transition to π_4 . The retraction phase is initiated as soon as the aircraft flies past w_{p1} which is defined as the outermost point on the path. This procedure ensures that before the reeling in of the tether is triggered the aircraft always has to fly downward through the center and flies towards the ground station on the same side of the wind window. Before the aircraft transitions back into the traction mode, one out of three conditions has to be satisfied: Either the tether length or the Euclidean distance $\|\mathbf{p}^G\|$ of the aircraft relatively to the ground station is below a specified value, or the elevation angle of the aircraft exceeds a maximum value. The latter can be regarded as a safety mechanism that prevents the aircraft from overshooting the ground station.

B. Guidance Modules

In the existing AWE literature [6, 21–23] the kite is steered according to the tangential plane course set point χ_τ . It is defined as the angle between the $\mathbf{e}_{x,\tau}$ axis of the tangential plane frame τ and the kinematic frame K as depicted in Fig. 1b. This strategy is mainly motivated by the fact that a direct relationship between the steering input of a flexible kite and the tangential plane course rate can be derived [8, 24] which allows to directly calculate the steering input based on the course rate. In this work the guidance problem will be solved as well by first calculating the desired χ_τ course set point, which will then however be transformed into a corresponding set point for the course χ_k and path angle γ_k , which specify the orientation of the K frame relatively to the O frame. This approach provides an additional control degree of freedom to track the desired flight direction. Moreover, controlling course and path angle in the traction phase allows to use the same medium loop control structure for the retraction phase in which the kite is not steered on a tangential plane anymore. Furthermore, providing set points for course and path angle allows to integrate the guidance module easier into existing autopilot architectures for conventional aircraft. Hence this approach also fits better into the modular

Table 1 State definitions.

State	Description
π_0	Transition from take-off to aircraft mode.
π_1	Capture crosswind pattern.
π_2	Traction phase.
π_3	Intermediate state between traction and transition.
π_4	Transition to retraction.
π_5	Retraction phase.

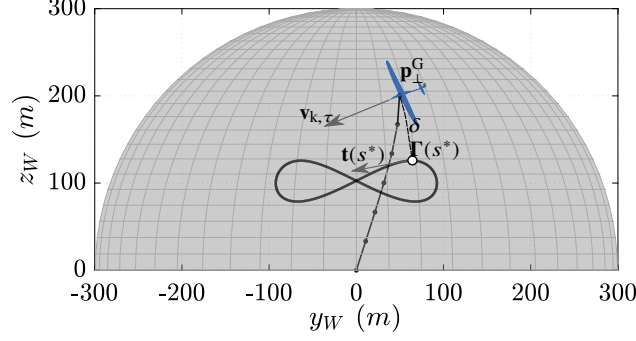


Fig. 4 Reference flight path on a sphere.

control philosophy proposed in this work.

1. Traction Phase Guidance

Separating the movement of the aircraft into a radial and a tangential movement the control objectives for the traction phase can be stated as follows: On the one hand, the radial direction needs to be controlled by the winch such that the tether force set point is tracked. Moreover, the radial direction controller needs to ensure that the maximum tether tension is not exceeded to avoid tether rupture or aircraft damage. For the tangential motion control the aircraft position will be projected onto the unit sphere. In that case, the flight controller needs to follow a predefined flight path on a sphere with a constant radius of one. The path on the unit sphere is adapted proportionally to the distance of the aircraft to the ground station such that the real path the aircraft traces has a constant shape during the reel-out phase. Fig. 4 depicts an example flight path, including a visualization of the aircraft and the flexible tether. Note that the depicted vectors and the aircraft model are scaled, and the physical flight path and not the path on the unit sphere that is used for the guidance is shown for visualization purposes.

The flow chart of the guidance module is depicted in Fig. 7. Note, only the course controller is depicted, the path angle controller is implemented analogously.

Parts of the guidance module are based on a previous work of the second author [8] where it is used to steer a flexible kite along a prescribed path. In this work some modifications are introduced such as a novel predictive part that takes the instantaneous path curvature into account in order to calculate the reference course rate. Furthermore, the interfaces to the aircraft path-following controller will be presented. Since the terminology slightly deviates from [8] the main steps of the derivation will be presented again in addition to the novel extensions.

As an overall objective of the guidance module it can be stated that the guidance law shall reduce the distance δ (i.e. the cross track error) as defined by the arc length between the projected aircraft position on the unit sphere \mathbf{p}_\perp^G and the path Γ , and for zero cross-track error the kinematic velocity vector projected onto the tangential plane $\mathbf{v}_{k,\tau}$ shall be aligned with the path direction as defined by the tangent vector \mathbf{t} . All vectors are depicted in Fig. 4. The path is defined in spherical coordinates on the unit sphere, hence a point on the path is fully defined by its longitude λ_Γ and latitude ϕ_Γ . Note, all vectors are given in the W reference frame, if not indicated otherwise. In Cartesian coordinates the path is given as

$$\mathbf{\Gamma}(s) = \begin{pmatrix} \cos \lambda_\Gamma(s) \cos \phi_\Gamma(s) \\ \sin \lambda_\Gamma(s) \cos \phi_\Gamma(s) \\ \sin \phi_\Gamma(s) \end{pmatrix} \quad (6)$$

For subsequent calculations the tangent and its derivative need to be known. The tangent can be calculated according to

$$\mathbf{t}(s) = \frac{d\mathbf{\Gamma}}{ds} = \frac{\partial \mathbf{\Gamma}}{\partial \lambda_\Gamma} \frac{d\lambda_\Gamma}{ds} + \frac{\partial \mathbf{\Gamma}}{\partial \phi_\Gamma} \frac{d\phi_\Gamma}{ds} \quad (7)$$

and its derivative is given by

$$\begin{aligned} \mathbf{t}'(s) = & \frac{\partial^2 \Gamma}{\partial \lambda_\Gamma^2} \left(\frac{d\lambda_\Gamma}{ds} \right)^2 + \\ & 2 \frac{\partial^2 \Gamma}{\partial \phi_\Gamma \partial \lambda_\Gamma} \frac{d\phi_\Gamma}{ds} \frac{d\lambda_\Gamma}{ds} + \frac{\partial^2 \Gamma}{\partial \phi_\Gamma^2} \left(\frac{d\phi_\Gamma}{ds} \right)^2 + \frac{\partial \mathbf{t}}{\partial s} \end{aligned} \quad (8)$$

The last partial derivative is given by

$$\frac{\partial \mathbf{t}}{\partial s} = \frac{\partial \Gamma}{\partial \lambda_\Gamma} \frac{d^2 \lambda_\Gamma}{ds^2} + \frac{\partial \Gamma}{\partial \phi_\Gamma} \frac{d^2 \phi_\Gamma}{ds^2} \quad (9)$$

Furthermore, the speed of the path parameter s is denoted with $ds/dt = \dot{s}$ and is given by the projection of the velocity vector

$$\frac{ds}{dt} = \dot{s} = \frac{\mathbf{t}^\top \mathbf{v}_{k,\tau}}{\|\mathbf{t}\|_2} \quad (10)$$

$\mathbf{v}_{k,\tau}$ is the normalized projection of $(\mathbf{v}_k^G)_W$ into the tangential plane τ given by

$$\mathbf{v}_{k,\tau} = \mathbf{V} (\mathbf{V}^\top \mathbf{V})^{-1} \mathbf{V}^\top \frac{(\mathbf{v}_k^G)_W}{\|(\mathbf{p}^G)_W\|} \quad (11)$$

where \mathbf{V} contains the basis vectors of the tangential plane frame:

$$\mathbf{V} = (\mathbf{e}_{x,\tau} \ \mathbf{e}_{y,\tau}) = \begin{pmatrix} -\sin \phi \cos \lambda & -\sin \lambda \\ -\sin \phi \sin \lambda & \cos \lambda \\ \cos \phi & 0 \end{pmatrix} \quad (12)$$

The flight path can be defined as a planar curve that is transformed into spherical coordinates using Eq. (6). The flight path in this work will be defined as a *Lemniscate of Booth*, given by

$$\lambda_\Gamma(s) = \frac{a_{\text{Booth}} \sin s}{1 + \left(\frac{a_{\text{Booth}}}{b_{\text{Booth}}} \right)^2 \cos^2 s}, \quad \phi_\Gamma(s) = \frac{\frac{a_{\text{Booth}}^2}{b_{\text{Booth}}} \sin s \cos s}{1 + \left(\frac{a_{\text{Booth}}}{b_{\text{Booth}}} \right)^2 \cos^2 s} \quad (13)$$

which can be derived from the equation of a hyperbolic lemniscate as defined for instance in [25, p.164] with $y = x \frac{a}{b} \cos s$. a_{Booth} and b_{Booth} are parameters that define height and width of the curve. A detailed comparison with other curve parameterizations is out of the scope of this paper.

The distance between a point on the curve and the kite position can be calculated using the definition of the arc length. Note, in the following all vectors are given in the W reference frame if not indicated otherwise:

$$\delta(s) = \arccos(\mathbf{p}_\perp^G \cdot \Gamma(s)) \quad (14)$$

In order to determine the closest point (defined by s^*) requires to solve

$$\left. \frac{d\delta}{ds} \right|_{s=s^*} = 0 \quad (15)$$

where the derivative is given by

$$\frac{d\delta}{ds} = -\frac{1}{\sin \delta} \frac{d(\mathbf{p}_\perp^G \cdot \Gamma(s))}{ds} = -\frac{\mathbf{p}_\perp^G \cdot \mathbf{t}(s)}{\sin \delta} \quad (16)$$

Eventually, the following root-finding problem needs to be solved:

$$\mathbf{p}_\perp^G \cdot \mathbf{t}(s) = 0 \quad (17)$$

the solution can be determined using for instance *Newton's* method. With

$$\left(\frac{d}{ds} \right) \mathbf{p}_\perp^G \cdot \mathbf{t}(s) = \mathbf{p}_\perp^G \cdot \frac{d\mathbf{t}(s)}{ds} \quad (18)$$

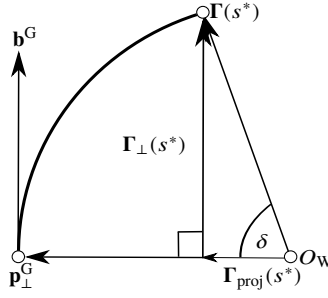


Fig. 5 A slice of the unit sphere containing a segment of the great circle that connects \mathbf{p}_{\perp}^G with $\Gamma(s^*)$.

The update equation for *Newton's* method is then

$$s^+ = s^- - \frac{\mathbf{p}_{\perp}^G \cdot \mathbf{t}(s)}{\mathbf{p}_{\perp}^G \cdot \mathbf{t}'(s)} \quad (19)$$

In the simulations, the method converged usually quickly after two to three iterations if the previous solution is selected as a starting point.

Knowing the closest point on the curve relative to the current aircraft position enables to calculate the desired flight direction. The vector at the current aircraft position pointing towards $\Gamma(s^*)$ perpendicularly along a great circle can be expressed as

$$\mathbf{b}^G = \frac{\Gamma(s^*) - \cos \delta \mathbf{p}_{\perp}^G}{\sin \delta} \quad (20)$$

This can be derived simply by looking at the normal projection of $\Gamma(s^*)$ onto \mathbf{p}_{\perp}^G (cf. Fig. 5) given by

$$\Gamma_{\text{proj}}(s^*) = \cos \delta \mathbf{p}_{\perp}^G \quad (21)$$

and

$$\Gamma_{\perp}(s^*) = \Gamma(s^*) - \Gamma_{\text{proj}}(s^*) \quad (22)$$

where $-\Gamma_{\perp}(s^*)$ denotes the vector of the projection direction, which is by definition perpendicular to \mathbf{p}_{\perp}^G . Normalizing $\Gamma_{\perp}(s^*)$ yields:

$$\mathbf{b}^G = \frac{\Gamma(s^*) - \Gamma_{\text{proj}}(s^*)}{\|\Gamma(s^*) - \Gamma_{\text{proj}}(s^*)\|_2} = \frac{\Gamma(s^*) - \cos \delta \mathbf{p}_{\perp}^G}{\sin \delta} \quad (23)$$

Equation (17) can be rewritten using Eq. (23):

$$\frac{\Gamma(s^*) \cdot \mathbf{t}(s^*) - \sin \delta (\mathbf{b}^G \cdot \mathbf{t}(s^*))}{\cos \delta} = 0 \quad (24)$$

The first scalar product is zero, since the position vector is perpendicular to the tangent vector, which yields

$$\tan \delta (\mathbf{b}^G \cdot \mathbf{t}(s^*)) = 0 \quad (25)$$

If this equation is divided by $\tan \delta$ and bearing in mind that the only relevant singularity is located at $\delta = 0$ this yields for $\delta \neq 0$

$$\mathbf{b}^G \cdot \mathbf{t}(s^*) = 0 \quad (26)$$

which proves that the direction vector pointing towards the path is indeed orthogonal to the tangent at $\Gamma(s^*)$. Practically speaking if the kite would fly in \mathbf{b}^G direction it would intercept the path perpendicularly.

From a practical point of view it is however not desired that the aircraft intercepts the path perpendicularly. Instead, it is desirable that the commanded flight direction smoothly transitions from an orthogonal interception if the aircraft is farther away from the curve to a tangential, hence curve aligned, flight direction. If the aircraft is on the path it is desired that the path controller tracks the directional angle of the tangent vector on the curve. If $\delta \neq 0$ the course angle

$\chi_{\tau,\parallel}$ has to be adapted such that the distance to the curve as measured by the arc-length decreases over time. In [8] the following set point definition is proposed, which is utilized in this work as well:

$$\chi_{\tau,c} = \chi_{\tau,\parallel} + \Delta\chi_{\tau} \quad (27)$$

with

$$\Delta\chi_{\tau} = \arctan\left(\frac{-\sigma(\iota)\delta}{\delta_0}\right) \quad (28)$$

and

$$\iota = (\mathbf{t}(s^*) \times \mathbf{\Gamma}(s^*)) \cdot (\mathbf{p}_{\perp}^G - \mathbf{\Gamma}(s^*)) \quad (29)$$

where σ denotes the sign of ι . Depending if the aircraft is on the left or right hand side of the path, as depicted in Fig. 6, the sign of $\Delta\chi_{\tau}$ is adapted accordingly.

If the course as defined in Eq. (27) is tracked by the flight control system, the relative distance δ between aircraft and path decreases over time, i.e. $\dot{\delta} < 0$. Taking the derivative of Eq. (14) with respect to time yields

$$\dot{\delta} = -\frac{1}{\sqrt{1 - \cos^2 \delta}} \left(\dot{\mathbf{p}}_{\perp}^G \cdot \mathbf{\Gamma}(s^*) + \mathbf{p}_{\perp}^G \cdot \dot{\mathbf{\Gamma}}(s^*) \right) \quad (30)$$

with

$$\dot{\mathbf{\Gamma}}(s^*) = \mathbf{t}(s^*)\dot{s} \quad (31)$$

$\mathbf{p}_{\perp}^G \cdot \mathbf{t}(s^*)$ is zero, therefore,

$$\dot{\delta} = -\frac{1}{\sin \delta} \left(\dot{\mathbf{p}}_{\perp}^G \cdot \mathbf{\Gamma}(s^*) \right) \quad (32)$$

With Eq. (23) the dot product can be written as

$$\dot{\mathbf{p}}_{\perp}^G \cdot \mathbf{\Gamma}(s^*) = \dot{\mathbf{p}}_{\perp}^G \cdot \mathbf{b}^G \sin \delta + \dot{\mathbf{p}}_{\perp}^G \cdot \mathbf{p}_{\perp}^G \cos \delta \quad (33)$$

Per definition, the second scalar product on the right hand side is zero. Inserting the result into Eq. (32) yields

$$\dot{\delta} = -\dot{\mathbf{p}}_{\perp}^G \cdot \mathbf{b}^G \quad (34)$$

This can be further simplified to

$$\dot{\delta} = -v_{k,\tau} \cos \theta \quad (35)$$

where $v_{k,\tau}$ is the magnitude of $\mathbf{v}_{k,\tau}$ and θ denotes the angle between the vector pointing perpendicularly to $\mathbf{\Gamma}(s^*)$ and the projected aircraft velocity on the tangential plane. To calculate θ two cases have to be distinguished:

$$\theta = \begin{cases} \pi/2 - \Delta\chi_{\tau} + e_{\chi_{\tau}}, & \text{for } \sigma < 0 \\ \pi/2 + \Delta\chi_{\tau} - e_{\chi_{\tau}}, & \text{for } \sigma > 0 \end{cases} \quad (36)$$

This yields for $\dot{\delta}$

$$\dot{\delta} = \begin{cases} -v_{k,\tau} \sin(\Delta\chi_{\tau} - e_{\chi_{\tau}}), & \text{for } \sigma < 0 \\ -v_{k,\tau} \sin(-\Delta\chi_{\tau} + e_{\chi_{\tau}}), & \text{for } \sigma > 0 \end{cases} \quad (37)$$

with Eq. (28) it follows

$$\dot{\delta} = \frac{-\sigma v_{k,\tau}}{\sqrt{1 + (\delta/\delta_0)^2}} \left(\sigma \delta / \delta_0 \cos e_{\chi_{\tau}} + \sin e_{\chi_{\tau}} \right) \quad (38)$$

where the identities $\sin(\arctan(x)) = x/\sqrt{1+x^2}$ and $\cos(\arctan(x)) = 1/\sqrt{1+x^2}$ have been utilized. If the course error dynamics are asymptotically stable i.e. $e_{\chi_{\tau}} \rightarrow 0$ then

$$\dot{\delta} = -v_{k,\tau} \frac{\delta/\delta_0}{\sqrt{1 + (\delta/\delta_0)^2}} \quad (39)$$

where the fact that $\sigma^2 = 1$ has been exploited. Equation (39) shows that if the commanded course according to Eq. (27) is tracked, the distance δ strictly decreases over time.

of the path-following controller. The derivative of $\chi_{\tau, \parallel}$ is given by

$$\dot{\chi}_{\tau, \parallel} = \frac{d}{dt} \arctan \left(\frac{\mathbf{e}_{y, \tau} \cdot \mathbf{t}^G}{\mathbf{e}_{x, \tau} \cdot \mathbf{t}^G} \right) \quad (44)$$

$$\dot{\chi}_{\tau, \parallel} = \frac{(\cos(\chi_{\tau, \parallel}) \quad -\sin(\chi_{\tau, \parallel})) \left(\left(\frac{\partial \mathbf{e}_{y, \tau}}{\partial \lambda} \dot{\lambda} + \frac{\partial \mathbf{e}_{y, \tau}}{\partial \phi} \dot{\phi} \right) \cdot \mathbf{t}^G + \mathbf{e}_{y, \tau} \cdot \frac{d\mathbf{t}^G}{ds} \dot{s} \right)}{\left(\left(\frac{\partial \mathbf{e}_{x, \tau}}{\partial \lambda} \dot{\lambda} + \frac{\partial \mathbf{e}_{x, \tau}}{\partial \phi} \dot{\phi} \right) \cdot \mathbf{t}^G + \mathbf{e}_{x, \tau} \cdot \frac{d\mathbf{t}^G}{ds} \dot{s} \right)} \quad (45)$$

with

$$\mathbf{e}_{x, \tau} = \begin{pmatrix} -\sin \phi \cos \lambda \\ -\sin \phi \sin \lambda \\ \cos \phi \end{pmatrix}, \quad \frac{\partial \mathbf{e}_{x, \tau}}{\partial \lambda} = \begin{pmatrix} \sin \phi \sin \lambda \\ -\sin \phi \cos \lambda \\ 0 \end{pmatrix}, \quad \frac{\partial \mathbf{e}_{x, \tau}}{\partial \phi} = \begin{pmatrix} -\cos \phi \cos \lambda \\ -\cos \phi \sin \lambda \\ -\sin \phi \end{pmatrix} \quad (46)$$

and

$$\mathbf{e}_{y, \tau} = \begin{pmatrix} -\sin \lambda \\ \cos \lambda \\ 0 \end{pmatrix}, \quad \frac{\partial \mathbf{e}_{y, \tau}}{\partial \lambda} = \begin{pmatrix} -\cos \lambda \\ -\sin \lambda \\ 0 \end{pmatrix}, \quad \frac{\partial \mathbf{e}_{y, \tau}}{\partial \phi} = \begin{pmatrix} 0 \\ 0 \\ 0 \end{pmatrix} \quad (47)$$

and

$$\dot{\lambda} = \frac{v_k^G}{\|(\mathbf{p}^G)_W\| \cos \phi}, \quad \dot{\phi} = \frac{u_k^G}{\|(\mathbf{p}^G)_W\|} \quad (48)$$

Equation (45) defines the rate with which the angle between the tangent vector \mathbf{t}^G defined by the path and the basis vector of the tangent plane frame $\mathbf{e}_{x, \tau}$ changes as the aircraft flies along the curve. It hence corresponds to the required course rate imposed by the path curvature.

2. Retraction Phase Guidance

The retraction phase guidance module is separated from the traction phase module. The supervisory logic switches to the retraction phase according to the high-level state machine status. The outputs of the retraction guidance module are again course and path angle commands. In contrast to the traction phase the aircraft will not follow a prescribed path but directly flies towards the zenith position with a predefined path angle. The path angle set point is given by a fixed descend angle, which is chosen manually. The course angle is calculated based on the relative position of the aircraft and the waypoint which is located at the zenith position of the small earth. The choice of this waypoint seems naturally because reeling in the tether will automatically pull the aircraft towards the zenith position. Additionally, in order to achieve a smoother transition back into the traction phase a *flare-like* maneuver is commanded that increases the descent rate linearly leading to a slight pull-up maneuver before the aircraft goes back into cross wind flight. The flare is initiated as a function of the aircraft latitude:

$$\gamma_{k, c} = \frac{\gamma_f - \gamma_i}{\phi_{\max} - \phi_0} (\phi - \phi_0) + \gamma_i \quad (49)$$

$$\bar{\gamma}_{k, c} = \max(\min(\gamma_{k, c}, \gamma_f), \gamma_i)$$

with $\phi_0 = \phi_{\max} - \Delta\phi$. The parameters $\Delta\phi$, γ_f , γ_i are chosen a manually by the operator and characterize the length of the flare, in terms of elevation angle, as well as the final and initial descent angle. The desired course angle is calculated based on the relative position of the aircraft and the origin of the wind frame:

$$\mathbf{b}_O^T = - \begin{pmatrix} p_{O, x} & p_{O, y} & 0 \end{pmatrix} \quad (50)$$

The course set point is then given by

$$\chi_{k, c} = \arctan_2(b_{O, y}, b_{O, x}) \quad (51)$$

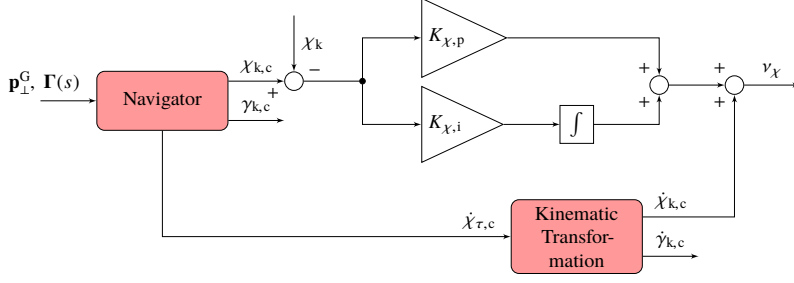


Fig. 7 Course controller block diagram.

C. Path Loop

1. Traction Phase

The lower level path-following controller requires the tangential plane course rate $\dot{\chi}_{\tau,c}$ as well as the desired flight direction defined by course and path angle $\chi_{k,c}$ and $\gamma_{k,c}$ from the guidance module in order to calculate the set points for the attitude controller consisting of aerodynamic bank angle $\mu_{a,c}$ as well as the angle of attack α_c . In order to be able to regulate course and path independently $\dot{\chi}_{\tau,c}$ will be converted into the corresponding course and path angle rates $\dot{\chi}_{k,c}$ and $\dot{\gamma}_{k,c}$, respectively. The tangential plane course rate occurs as the z component of the angular velocity vector between the τ and the \bar{K} frame given in the rotated kinematic frame \bar{K} :

$$\left(\omega^{\tau\bar{K}}\right)_{\bar{K}}^T = \begin{pmatrix} 0 & 0 & \dot{\chi}_{\tau} \end{pmatrix}_{\bar{K}} \quad (52)$$

The \bar{K} frame represents the rotated kinematic frame such that the x and the y component of the K frame are in the tangent plane τ , hence the $z_{\bar{K}}$ axis is aligned with the z_{τ} axis of the τ -frame. $\left(\omega^{\tau\bar{K}}\right)_{\bar{K}}$ can be converted using the kinematic relations between the reference frames into the angular velocity vector between the O and \bar{K} frame, denoted with $\left(\omega^{O\bar{K}}\right)_{\bar{K}}$.

$$\left(\omega^{O\bar{K}}\right)_{\bar{K}} = \mathbf{M}_{\bar{K}O} \left(\left(\omega^{OW}\right)_O + \mathbf{M}_{OW} \left(\omega^{W\tau}\right)_W \right) + \left(\omega^{\tau\bar{K}}\right)_{\bar{K}} \quad (53)$$

It is reasonable to assume that the mean wind direction changes much slower than the transport rate $\left(\omega^{W\tau}\right)_W$ and the course rate vector $\left(\omega^{\tau\bar{K}}\right)_{\bar{K}}$ hence $\left(\omega^{OW}\right)_K$ can be set to zero. This yields

$$\left(\omega^{O\bar{K}}\right)_{\bar{K}} = \mathbf{M}_{\bar{K}O} \mathbf{M}_{OW} \left(\omega^{W\tau}\right)_W + \left(\omega^{\tau\bar{K}}\right)_{\bar{K}} = \begin{pmatrix} \dot{\mu}_k - \dot{\chi}_{k,c} \sin \gamma_k \\ \dot{\gamma}_{k,c} \cos \mu_k + \dot{\chi}_{k,c} \sin \mu_k \cos \gamma_k \\ -\dot{\gamma}_{k,c} \sin \mu_k + \dot{\chi}_{k,c} \cos \mu_k \cos \gamma_k \end{pmatrix}_{\bar{K}} \quad (54)$$

with

$$\left(\omega^{W\tau}\right)_W^T = \begin{pmatrix} \dot{\phi} \sin \lambda & -\dot{\phi} \cos \lambda & \dot{\lambda} \end{pmatrix}_W \quad (55)$$

The transformation matrix $\mathbf{M}_{\bar{K}O}$ can be calculated using the knowledge of course and path angle as well as the position of the aircraft in the W frame. With

$$\mathbf{e}_{x,\bar{K},O} = \begin{pmatrix} \cos \chi_k \cos \gamma_k \\ \sin \chi_k \cos \gamma_k \\ -\sin \gamma_k \end{pmatrix}, \mathbf{e}_{z,\bar{K},O} = -\mathbf{M}_{OW} \left(\mathbf{p}^G\right)_W, \mathbf{e}_{y,\bar{K},O} = \mathbf{e}_{z,\bar{K},O} \times \mathbf{e}_{x,\bar{K},O} \quad (56)$$

this yields

$$\mathbf{M}_{\bar{K}O} = \begin{pmatrix} \mathbf{e}_{x,\bar{K},O}^T \\ \mathbf{e}_{y,\bar{K},O}^T \\ \mathbf{e}_{z,\bar{K},O}^T \end{pmatrix} \quad (57)$$

The course rate and the path angle rate can then be calculated according to

$$\dot{\chi}_{k,c} = \frac{\omega_{y,\bar{K}}^{O\bar{K}} \sin \bar{\mu} + \omega_{z,\bar{K}}^{O\bar{K}} \cos \bar{\mu}}{\cos \gamma_k}, \quad \dot{\gamma}_{k,c} = \omega_{y,\bar{K}}^{O\bar{K}} \cos \bar{\mu} - \omega_{z,\bar{K}}^{O\bar{K}} \sin \bar{\mu} \quad (58)$$

with

$$\bar{\mu} = \arctan\left(\frac{M_{\bar{K}O,32}}{M_{\bar{K}O,33}}\right) \quad (59)$$

Besides the feed forward part for the course and path angle rate also a feedback part is added. The overall pseudo control inputs are then given by

$$\begin{aligned} v_\chi &= \dot{\chi}_{k,c} + k_{p,\chi} (\chi_{k,c} - \chi_k) + k_{i,\chi} \int_0^t (\chi_{k,c} - \chi_k) d\tau \\ v_\gamma &= \dot{\gamma}_{k,c} + k_{p,\gamma} (\gamma_{k,c} - \gamma_k) + k_{i,\gamma} \int_0^t (\gamma_{k,c} - \gamma_k) d\tau \end{aligned} \quad (60)$$

The set points of the attitude controller will be derived using a model for the path dynamics. The total acceleration of the aircraft in the kinematic frame is given by:

$$(\dot{\mathbf{v}}_k)_K^O = \begin{pmatrix} \dot{v}_k \\ 0 \\ 0 \end{pmatrix}_K + (\boldsymbol{\omega}^{OK})_K \times \begin{pmatrix} v_k \\ 0 \\ 0 \end{pmatrix}_K = \begin{pmatrix} \dot{v}_k \\ \dot{\chi}_k \cos \gamma_k v_k \\ -\dot{\gamma}_k v_k \end{pmatrix}_K = \begin{pmatrix} a_{x,K} \\ a_{y,K} \\ a_{z,K} \end{pmatrix}_K \quad (61)$$

Which yields the path dynamics:

$$m \begin{pmatrix} a_{x,K} \\ a_{y,K} \\ a_{z,K} \end{pmatrix}_K = (\mathbf{F}_a)_K + (\mathbf{F}_g)_K + (\mathbf{F}_t)_K \quad (62)$$

involving the aerodynamic force $(\mathbf{F}_a)_K \in \mathbb{R}^{3 \times 1}$, gravitational force $(\mathbf{F}_g)_K \in \mathbb{R}^{3 \times 1}$ as well as the tether force $(\mathbf{F}_t)_K \in \mathbb{R}^{3 \times 1}$ in the K frame, where gravity and tether force are given by

$$(\mathbf{F}_g)_K^\top = \begin{pmatrix} -\sin \phi m_k g & 0 & \cos \phi m_k g \end{pmatrix} \quad (63)$$

and

$$(\mathbf{F}_t)_K = -\mathbf{M}_{KO} \frac{(\mathbf{p})_O}{\|(\mathbf{p})_O\|_2} F_t \quad (64)$$

Solving for the aerodynamic force yields

$$\begin{pmatrix} \bar{f}_{x,K} \\ \bar{f}_{y,K} \\ \bar{f}_{z,K} \end{pmatrix}_K = m \begin{pmatrix} a_{x,K} \\ a_{y,K} \\ a_{z,K} \end{pmatrix}_K - (\mathbf{F}_g)_K - (\mathbf{F}_t)_K = (\mathbf{F}_a)_K \quad (65)$$

The last two rows can be written as

$$\begin{aligned} \bar{f}_{y,K} &= \cos \mu_k f_{a,y,\bar{K}} - \sin \mu_k f_{a,z,\bar{K}} \\ \bar{f}_{z,K} &= \sin \mu_k f_{a,y,\bar{K}} + \cos \mu_k f_{a,z,\bar{K}} \end{aligned} \quad (66)$$

with

$$\begin{aligned} f_{a,y,\bar{K}} &= -\cos \alpha_k \sin \beta_k f_{a,x,B} + \cos \beta_k f_{a,y,B} - \sin \alpha_k \sin \beta_k f_{a,z,B} \\ f_{a,z,\bar{K}} &= -\sin \alpha_k f_{a,x,B} + \cos \alpha_k f_{a,z,B} \end{aligned} \quad (67)$$

Note that α_k and β_k are the kinematic angle of attack and kinematics sideslip angle. Since the inner loop controller actively controls the sideslip angle β , i.e. the aerodynamic sideslip angle, the aerodynamic side force $f_{a,y,B}$ is approximately zero. Contrarily, the kinematic sideslip angle β_k is in presence of wind not zero. Hence,

$$\begin{aligned} f_{a,y,\bar{K}} &= -\cos \alpha_k \sin \beta_k f_{a,x,B} - \sin \alpha_k \sin \beta_k f_{a,z,B} \\ f_{a,z,\bar{K}} &= -\sin \alpha_k f_{a,x,B} + \cos \alpha_k f_{a,z,B} \end{aligned} \quad (68)$$

The set point for the kinematic bank angle based on the required course and path angle rate is calculated by solving Eq. (66) for μ_k and inserting the pseudo control signals for the course and path angle rates:

$$\mu_{k,c} = \arctan_2 \left(\frac{m_k v_\chi \cos \gamma_k v_k - f_{t,y,K}}{m_k v_\gamma v_k + m_k g \cos \gamma_k + f_{t,z,K}} \right) + \arctan \left(\frac{\bar{f}_{a,y,\bar{K}}}{\bar{f}_{a,z,\bar{K}}} \right) \quad (69)$$

which requires estimates for the aerodynamic forces $\bar{f}_{a,y,\bar{K}}$ and $\bar{f}_{a,z,\bar{K}}$.

Based on the set point for the kinematic banking angle the corresponding Euler roll angle can be calculated according to

$$\Phi_c = \arcsin \left(\frac{\cos \gamma_k \cos \beta_k (\sin \mu_{k,c} - \tan \gamma_k \tan \beta_k)}{\cos \Theta} \right) \quad (70)$$

Equation (70) can be obtained by comparing the relevant coefficients of $\mathbf{M}_{B\tau} = \mathbf{M}_{BO} \mathbf{M}_{OW} \mathbf{M}_{W\tau}$. The matrix \mathbf{M}_{BO} is obtained for instance from [12, p. 12]. The matrix $\mathbf{M}_{W\tau}$ is equivalent to the transformation from the Earth-Centered-Earth-Fixed (E) frame into the O frame (cf. [12, p. 31]) where the E frame corresponds to the W frame and the O frame corresponds to the τ frame. \mathbf{M}_{OW} is given by

$$\mathbf{M}_{OW} = \begin{pmatrix} \cos \xi & \sin \xi & 0 \\ \sin \xi & -\cos \xi & 0 \\ 0 & 0 & -1 \end{pmatrix} \quad (71)$$

where ξ denotes the wind direction measured from the north direction. Note, the structure of $\mathbf{M}_{B\tau}$ is equivalent to the structure of \mathbf{M}_{BO} . Φ_c can then be transformed into an aerodynamic banking angle command $\mu_{a,c}$ using Eq. (72).

$$\mu_{a,c} = \arcsin \left(\frac{\cos \Theta \sin \Phi}{\cos \gamma_a \cos \beta} + \tan \gamma_a \tan \beta_a \right) \quad (72)$$

The required aerodynamic path angle can be calculated using Eq. (73), which has been derived in [13, p. 20-23].

$$\gamma_a = \arcsin \left(\frac{v_k \sin \gamma_k + v_{w,O,z}}{v_a} \right) \approx \arcsin \left(\frac{v_k \sin \gamma_k}{v_a} \right) \quad (73)$$

Notice that, the calculation of γ_a requires the knowledge of the wind component in z_O direction $v_{w,O,z}$ which is however usually negligibly small compared to the horizontal components. The angle of attack set point can be calculated similarly to the approach presented in [26] with

$$L_{\text{req}} \approx \sqrt{\bar{f}_{y,K}^2 + \bar{f}_{z,K}^2} \quad (74)$$

Note, due to the wind influence this is only an approximation which is neglected in [26]. In fact, since the available traction force needs to be maximized it makes sense to choose a fixed set point during the traction phase close to the maximum angle of attack. Note, a maneuver might require less lift to achieve a desired curvature, hence choosing an arbitrary angle of attack would not allow to track the path rate commands in untethered flight. However, in the present case the kinematic constraint imposed by the tether length allows to automatically convert the excess in lift into additional traction force.

Due to the saturation of the angle of attack the actual responses in terms of the course rate and path angle rate are different to the commanded rates. This can lead to a windup of the integrators in the path loop. One approach to mitigate the windup is to adapt the reference model by the control deficit that results from the saturation (i.e. pseudo control hedging, PCH). However, for the traction phase controller the reference course rate is directly calculated based on the path geometry, as discussed in the previous section. This prevents a standard implementation of PCH, since no reference filter is used. Instead, an anti-windup scheme based on *back-calculation* is used, where the the feedback part corresponds again to the deficit between for instance the commanded course rate $v_{\chi,k,c}$ and the expected course rate $\dot{\chi}_{k,c}$. The hedge signal is then defined by

$$v_{h,\chi} = k_{bc} (v_{\chi,k,c} - \dot{\chi}_{k,c}) \quad (75)$$

The gain k_{bc} is chosen to be smaller than the integrator gain, as recommended in [27, pp. 79-80]. The feedback law for the pseudo control input is then adapted according to

$$v_\chi = \dot{\chi}_{k,c} + k_{p,\chi} (\chi_{k,c} - \chi_k) + k_{i,\chi} \int_0^t (\chi_{k,c} - \chi_k - v_{h,\chi}) d\tau \quad (76)$$

The adaption of the flight path rate channel follows analogously.

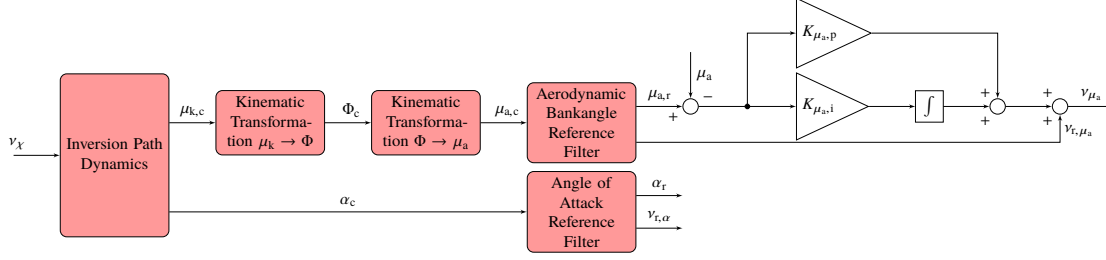


Fig. 8 Path and attitude loop block diagram.

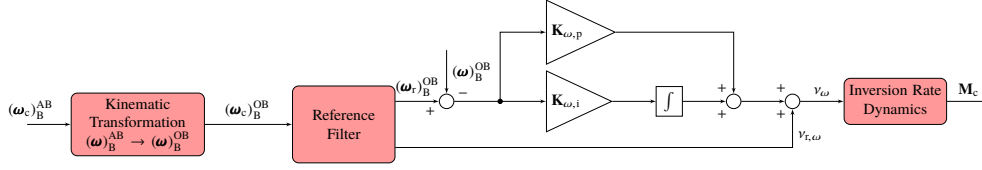


Fig. 9 Rate loop block diagram.

2. Retraction Phase

The course and path angle controller are designed similarly to the traction phase controller, the only difference consists of the calculation of the course and path angle rate commands. Since in the retraction phase no defined path needs to be followed, the rate commands are generated with a second order reference filters. Although first order filters would be sufficient second order filters lead to an additional smoothing of the derivative [28]. Instead of using a back-calculation anti-windup scheme a conventional PCH approach is chosen using estimates for the feasible course and path angle rates. With the hedging signal v_h the equations of the second order filter in case of the course loop are defined by

$$\begin{aligned} \dot{v}_{r,\chi} &= -2\zeta\omega_0 v_{r,\chi} + \omega_0^2 (\chi_{k,c} - \chi_{k,r}) \\ \dot{\chi}_{k,r} &= v_{r,\chi} - v_h \end{aligned} \quad (77)$$

and an equivalent pseudo control law with PI controller as for the traction phase is used. Note, in contrast to a fixed value for the angle of attack set point, the approximate expression of the required lift in Eq. (74) is used to determine the corresponding lift coefficient and by inversion of the lift coefficient the angle of attack set point α_c is determined. The control laws for the attitude and rate loop are implemented analogously to the traction phase loops.

D. Attitude Loop

The pseudo control inputs for the attitude to rate inversion are given by

$$\begin{aligned} v_{\mu_a} &= v_{r,\mu_a} + K_{\mu,p} (\mu_{a,r} - \mu_a) + K_{\mu,i} \int_0^t (\mu_{a,r} - \mu_a) d\tau \\ v_{\alpha} &= v_{r,\alpha} + K_{\alpha,p} (\alpha_r - \alpha) + K_{\alpha,i} \int_0^t (\alpha_r - \alpha) d\tau \\ v_{\beta} &= K_{\beta,p} (\beta_r - \beta) + K_{\beta,i} \int_0^t (\beta_r - \beta) d\tau \end{aligned} \quad (78)$$

where v_{r,μ_a} and $v_{r,\alpha}$ are calculated with a equivalent reference filter as defined for the course angle in Eq. (77). The inversion of the attitude to rate dynamics is purely kinematic and given by

$$\left(\boldsymbol{\omega}_c^{\text{OB}}\right)_B = \mathbf{M}_{B\bar{A}} \begin{pmatrix} -\dot{\chi}_a \sin \gamma_a \\ \dot{\gamma}_a \\ \dot{\chi}_a \cos \gamma_a \end{pmatrix}_{\bar{A}} + \left(\boldsymbol{\omega}^{\bar{A}B}\right)_B \quad (79)$$

with

$$\left(\boldsymbol{\omega}^{\bar{A}B}\right)_B = \begin{pmatrix} \cos \alpha \cos \beta v_\mu + v_\beta \sin \alpha \\ \sin \beta v_\mu + v_\alpha \\ \sin \alpha \cos \beta v_\mu - \cos \alpha v_\beta \end{pmatrix}_B \quad (80)$$

The matrix $\mathbf{M}_{\bar{A}B}$ is defined in for instance [14, p. 62]. $\dot{\chi}_a$ and $\dot{\gamma}_a$ are estimated by filtering Eq. (73) and Eq. (81), as derived in [13, p. 23]

$$\chi_a = \chi_k + \beta - \arcsin \left(\frac{1}{V_a \cos \gamma_a} (v_{w,O,y} \cos \chi_{k,c} - v_{w,O,x} \sin \chi_{k,c}) \right), \quad (81)$$

using a washout-filter, as proposed in [29]:

$$G(s) = \frac{s\omega_f^2}{s^2 + 2\omega_f s + \omega_f^2} \quad (82)$$

where $\omega_f = 90$ the filter bandwidth. Note, a better accuracy could be achieved by calculating $\dot{\chi}_{k,c}$ and $\dot{\gamma}_{k,c}$ analytically using the model of the course and path rate dynamics as defined in Eq. (62) and only filter the remaining terms.

E. Rate Loop

Note, since it is assumed that the tether is connected close to the center of gravity of the aircraft the rate loop of the tethered aircraft can be implemented analogously to the rate loop of a conventional aircraft. In the literature there exists an ample amount of different approaches to control the rate dynamics of aircraft, in this work a conventional first order dynamic inversion controller with second order reference filters and an incremental control allocation as presented in [26] is used. Note, the incremental approach is necessary since in general the relationship between actuator inputs and aerodynamic moments is nonlinear and not globally invertible. Since up to now and in the future extensive effort is and will be put into the modeling and identification of the AWE system, a model-based inversion is chosen over a sensor-based inversion as for instance presented in [30].

The commanded attitude rates as calculated by Eq. (79) are filtered and the resulting rate accelerations are added to a PI control part analogously to Eq. (78) yielding the pseudo-control input to the rate-dynamic inversion. From the resulting moment the current acting moment on the aircraft, estimated using a model, is subtracted yielding the required moment increment to track the commanded rates:

$$\begin{pmatrix} \Delta L \\ \Delta M \\ \Delta N \end{pmatrix} = \begin{pmatrix} L_c \\ M_c \\ N_c \end{pmatrix} - \begin{pmatrix} L_0 \\ M_0 \\ N_0 \end{pmatrix} = \mathbf{J} \boldsymbol{\omega} + \left(\boldsymbol{\omega}\right)_B^{\text{OB}} \times \mathbf{J} \left(\boldsymbol{\omega}\right)_B^{\text{OB}} - \begin{pmatrix} L_0 \\ M_0 \\ N_0 \end{pmatrix}. \quad (83)$$

Eventually, the moment increments are mapped to a surface deflection increment that is added to the current surface deflection resulting in the final actuator command:

$$\begin{pmatrix} \delta_{a,c} \\ \delta_{e,c} \\ \delta_{r,c} \end{pmatrix} = \begin{pmatrix} \delta_{a,0} \\ \delta_{e,0} \\ \delta_{r,0} \end{pmatrix} + \begin{pmatrix} \Delta \delta_a \\ \Delta \delta_e \\ \Delta \delta_r \end{pmatrix} = \begin{pmatrix} \delta_{a,0} \\ \delta_{e,0} \\ \delta_{r,0} \end{pmatrix} + \begin{pmatrix} C_{l\delta_a} & 0 & C_{l\delta_r} \\ 0 & C_{m\delta_e} & 0 \\ C_{n\delta_a} & 0 & C_{n\delta_r} \end{pmatrix} \begin{pmatrix} \Delta L \\ \Delta M \\ \Delta N \end{pmatrix}, \quad (84)$$

where $C_{i,j}$ represents a roll- (L), pitch- (M) or yaw-moment (N) control derivative that are obtained by linearizing the aerodynamic moment model with respect to the control surface deflections.

F. Winch Controller

The winch controller is derived based on the model defined in Eq. (5). At this stage of the work the winch controller is derived without explicitly taking into account the aircraft dynamics as presented for instance in [31]. The reason

is that if the aircraft dynamics are taken into account, the full state vector of the aircraft has to be available to the winch controller. So far no reliable information about the communication between the aircraft and the ground station is available, hence it is decided to control the winch only based on the measured tether force on the ground. In AWE, two high level control objectives for the winch controller can be formulated. First, the net power output has to be maximized by controlling the radial motion of the aircraft in an optimal way, second, since no on-board propulsion is available the winch can be used to control the airspeed by adapting the reeling speed. This allows to mitigate the effect of sudden wind speed and hence airspeed changes due to gusts. In this work, the focus will lay on the second control object, since the performance of the airspeed controller has a significant impact on the overall robustness of the control system which obviously is a prerequisite for optimal power output.

Note, from the perspective of the winch, the dynamics of the aircraft and the tether represent a disturbance that the winch controller needs to regulate in order to track a force set point. If a tether force measurement on the ground is available, which is usually the case in this application, a complex disturbance model is not necessary because all relevant information is condensed in the force measurement. The set point for the reeling speed can then be derived as follows. The aircraft dynamics in the tangential plane, or spherical coordinates, are given by

$$\left(\dot{\mathbf{v}}^G\right)_\tau + (\boldsymbol{\omega})_\tau^{W\tau} \times \left(\mathbf{v}^G\right)_\tau = \frac{\left(\mathbf{F}_g\right)_\tau + \left(\mathbf{F}_a\right)_\tau + \left(\mathbf{F}_t\right)_\tau}{m_k} \quad (85)$$

Assuming a straight tether only the third row is relevant which is given by

$$\dot{v}_{z,\tau} = -\omega_x v_{y,\tau} + \omega_y v_{x,\tau} + \frac{F_{g,z,\tau} + F_{a,z,\tau} + F_t}{m_k} \quad (86)$$

This can be written more compactly as

$$\dot{v}_{z,\tau} = \frac{F_{\text{aircraft}} + F_t}{m_k} \quad (87)$$

with

$$F_{\text{aircraft}} = m_k \left(-\omega_x v_{y,\tau} + \omega_y v_{x,\tau} \right) + F_{g,z,\tau} + F_{a,z,\tau} \quad (88)$$

Note, F_{aircraft} requires the knowledge of the full aerodynamic model of the aircraft as well as the relevant measured states if used for the set point calculation. However, instead of an estimation of F_{aircraft} the measured tether force on the ground can be used, since it can be assumed that $F_{\text{aircraft}} \approx -F_{t,m}$. If the tether is straight, the reeling speed v_r is equal to $-v_{z,\tau}$, hence

$$\dot{v}_r = \frac{F_{t,m} - F_t}{m_k} \quad (89)$$

If F_t is then replaced by the desired traction force $F_{t,c}$ the resulting acceleration can be interpreted as a reference acceleration proportional to the tether force tracking error. With $\dot{\omega}_w = \dot{v}_r/r_w$ this expression can be substituted into the winch model in Eq. (5) and solved for the reference torque:

$$M_c = \left(\frac{J_w}{r_w m_k} - r_w \right) F_{t,m} - \frac{J_w}{r_w m_k} F_{t,c} \quad (90)$$

Substituting this expression back into the winch model yields the closed loop winch model

$$\dot{\omega}_w = \frac{1}{r_w m_k} (F_{t,m} - F_{t,c}) + \Delta_w \quad (91)$$

where Δ_w is the model mismatch as a result of an imperfect inversion of the plant dynamics. Note, if the measured tether force deviates from the set point the winch will reel out faster or slower. Although simple, this approach proved to be highly effective in dealing with varying wind conditions and wind gusts as will be shown in section IV, while being independent of any aircraft specific parameters or aircraft states. In order to get rid of steady state errors an integrator term $k_i \int_0^t F_m - F_{t,s} d\tau$ can be added to Eq. (90). For the stability of Eq. (91) only a qualitative, but highly intuitive stability proof is given. If the tether force becomes larger than the set point force the winch will start to accelerate according to Eq. (91). Of course this is strictly only true if $\frac{1}{r_w m_k} (F_m - F_{t,s}) > \Delta_w$. However, in the opposite case the acceleration will only be delayed, since if the winch further decelerates the tension in the tether would increase steadily until the tracking error contribution will be larger than Δ_w . If the winch accelerates the kinematic radial speed

of the aircraft will increase which decreases the apparent wind speed. As a consequence the lift force will drop, which decreases the tension in the tether and therefore decreases the tether force tracking error. The causal chain holds of course for the opposite case as well, where the tether force is smaller than the force set point. As an additional safety mechanism a speed controller is implemented that is also used during the retraction phase. In case of a sudden drop or increase in tether force beyond a defined threshold the set point for the reeling out speed is set to a constant positive value (e.g. 5 m/s) to decrease the tension in the tether rapidly by fast reeling out of the tether, or by reeling in rapidly if the tether force drops below the minimum value. During the retraction phase the reeling in speed is set to a fixed value, usually the maximum reeling in speed that the winch can achieve is chosen in order to minimize the retraction time. For the tracking task of the speed controller a dynamic model based feed forward controller (cf. [32, pp. 324-328]) for fast tracking is combined with a linear quadratic feedback regulator with servomechanism [33, pp. 51-62]. The prefilter is recommended since the set point commands for the reeling speed can jump which are then smoothed by the filter. Additionally, a feed-forward disturbance compensation is added since from the perspective of the speed controller the tether force represents a measurable disturbance.

IV. Results

In this section two different simulation setups are used to investigate the robustness of the control system. First, the robustness with respect to modest changes in the wind speed due to turbulence and wind shear is assessed. In the second part, the effect on the control performance of sudden and significant wind speed changes caused by gusts is analyzed.

A. Consecutive Pumping Cycles in a Turbulent Wind Field

Fig. 10a and Fig. 10b show the resulting flight path projected into the $x_W z_W$ and $x_W y_W$ plane. Fig. 11 depicts the path projected into the tangential plane at $\lambda = 0^\circ$ and $\phi = \phi_0$ (center of the figure of eight). Despite the turbulent wind field, shown in Fig. 14b, the control system is able to guide the aircraft along the defined flight path reliably. The visible deviations between the reference path and the real flight path are acceptable and are caused by the limited bandwidth of the control system. This limitation results in a repetitive non-zero cross track error during the turns. In the displayed results roughly three consecutive pumping cycles were flown. The reoccurring flight patterns demonstrate the robustness of the closed loop system towards modest changes in wind speed caused by wind shear and turbulence.

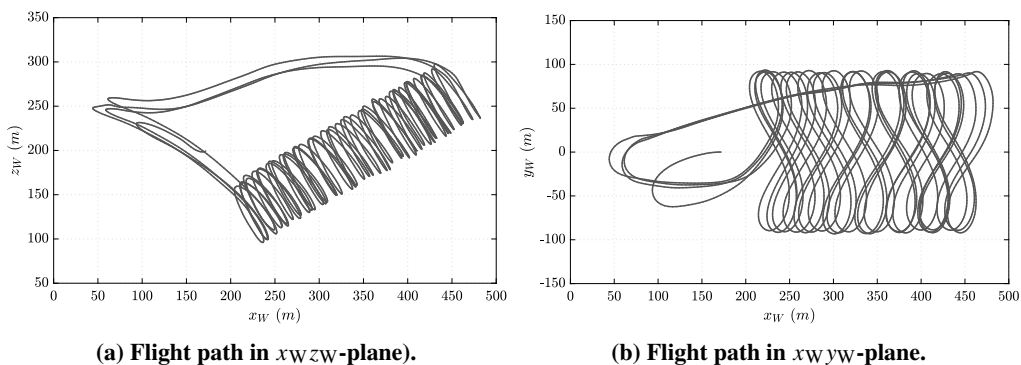


Fig. 10 Flight path during three consecutive pumping cycles.

As described in section III, reference filters are used to generate the course and path angle rates during the retraction phase. This allows to implement PCH to adapt the reference filters in case of saturation of the control signal. From the point of view of the path loop, the control signals are the bank angle command $\mu_{a,c}$ as well as the angle of attack command α_c . In Fig. 13a it can be observed that during a significant part of the retraction phase, e.g. for instance between 239 s and 246 s, the angle of attack is saturating. In this case the commanded pseudo-control inputs v_γ and v_χ will deviate from the actual plant responses. The adaptation of the course and path angle reference filters can be observed in Fig. 12a and Fig. 12b. The effect is especially visible for the path angle whose primary control variable is the angle of attack. The reference path angle first increases as a result of the hedge signal, reaching a maximum value of 30° before it decreases and eventually converges towards the negative commanded set point $\gamma_{k,c}$. Note, the deviations after 249 s are due to the continues change of $\gamma_{k,c}$ during the pull-up maneuver at the end of the retraction phase.

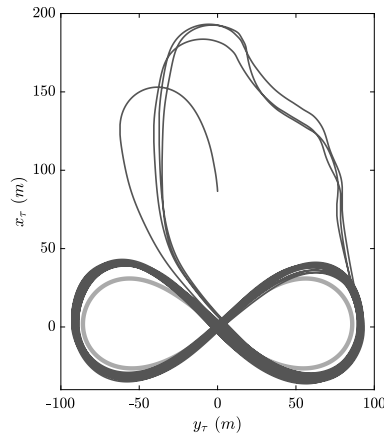


Fig. 11 Figure of eight flight path projection.

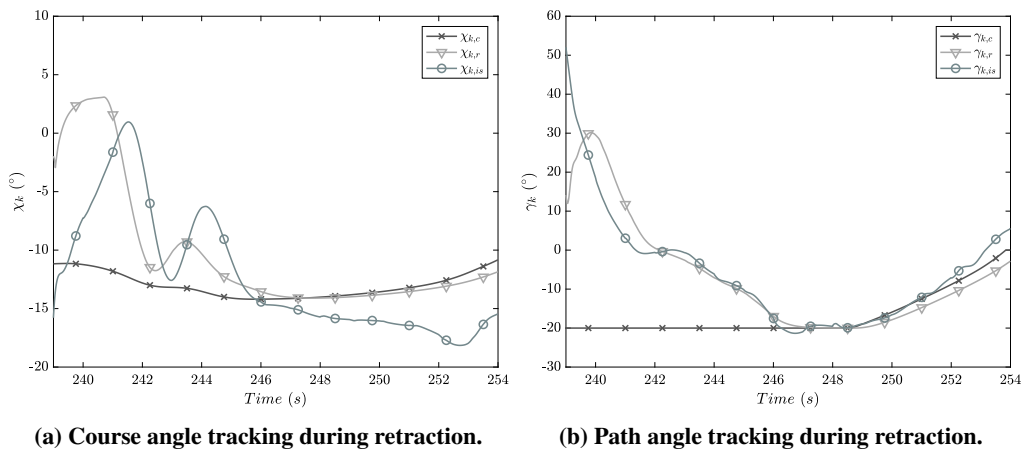
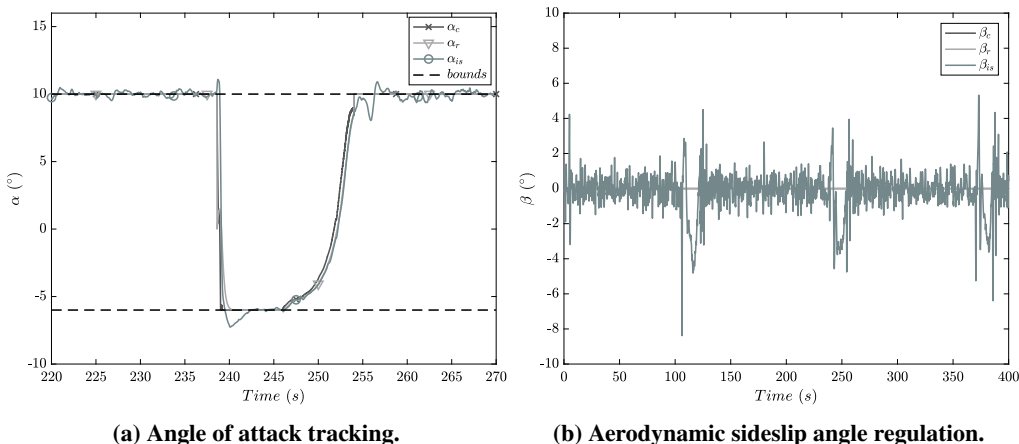


Fig. 12 Evolution of the path angles during the retraction phase.

During the pumping cycles the sideslip angle varies most of the time between -2° to $+2^\circ$. Larger sideslip angles occur during the transition phases from traction into retraction and vice versa as can be seen in Fig. 13b.

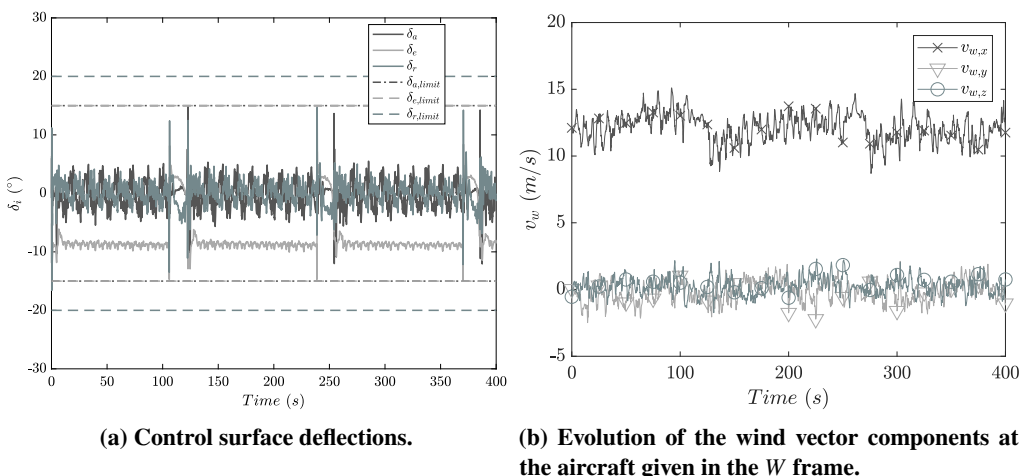
The evolution of the aircraft control surface deflections is depicted in Fig. 14a. It can be observed that the highest control effort is required in the transition phases where the control surfaces partially saturate. During the traction phases the aileron and rudder inputs vary in a repetitive manner between -5° to $+5^\circ$ while the rudder deflections remains almost constant at around -9° as a results of the fixed angle of attack set point during the traction phase.

Besides the analysis of the flight control performance the winch control performance needs to be assessed. Fig. 15a shows the evolution of the tether force as measured on the ground. During the conducted simulations a tether force set point of 1000 N is chosen, which is well beyond the structural limitations of around 1500 N. It can be observed that the tether force oscillates around the set point with an amplitude of around 50 N to 100 N. The oscillations are a result of the continues acceleration and deceleration of the aircraft while flying down and upwards during the figure of eight flight. To further reduce these oscillations an improved feed-forward winch controller could be implemented in the future that systematically reels out slower during upward and faster during downward flight. At the moment this is partially achieved via feedback control of the tether force. Furthermore, the resulting variations in the reeling speed depicted in Fig. 15b should be reduced in the future since variations in reeling speed would lead to large oscillations in the mechanical power output in combination with a constant tether force. One option to tackle this problem would be to use the pitch channel of the aircraft to control the airspeed, which is out of the scope of this paper.



(a) Angle of attack tracking.

(b) Aerodynamic sideslip angle regulation.

Fig. 13 Angle of attack and sideslip tracking.

(a) Control surface deflections.

(b) Evolution of the wind vector components at the aircraft given in the W frame.**Fig. 14** Actuator signals and turbulent wind field.

B. Robustness towards Wind Gusts

In this section the robustness of the control system towards rapid changes in the mean wind speed will be analyzed. For that purpose a *mexican hat* gust as defined in [34] is implemented and activated during the simulation at a specified instant in time. In this work only the response of the aircraft towards gusts in up- and downwind direction as depicted in Fig. 16 is analyzed.

In both cases the gust leads to a significant increase or decrease in airspeed and therefore tether force. In order to keep the tether force around the set point (cf. Fig. 20) the winch controller has to adapt the reeling out speed according to Eq. 90 (cf. Fig. 19). It can be observed that the reeling speed change follows the shape of the gust proportionally. Figure 17 shows the effect of this gust-load alleviation strategy in the radial direction. The flight path gets compressed (Fig. 18a) or stretched (Fig. 18b) depending on the gust direction as a result of the increasing or decreasing reeling out velocity. In Fig. 17 the resulting deviation from the nominal path following performance is barely visible in both cases.

V. Conclusion

In this paper a novel modular model based control architecture for rigid-wing airborne wind energy systems operated in pumping-cycle mode has been presented. The presented control approach leads to a robust control performance while flying in a realistic turbulent wind field. The extended geometric path-following approach guided the aircraft along a three dimensional curve reliably. State and input constraints are systematically handled using pseudo control hedging, which turns out to be beneficial especially during the retraction phase where the commanded flight path is adapted

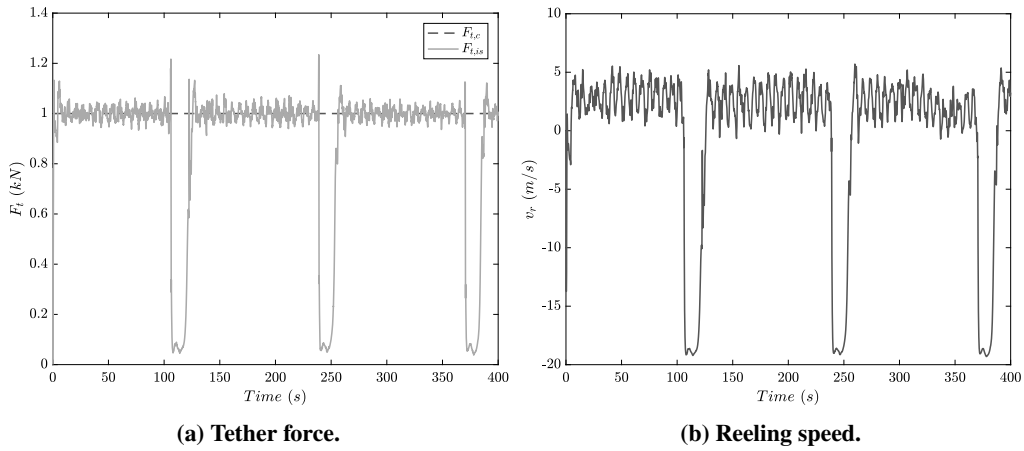


Fig. 15 Tether force tracking and reeling speed.

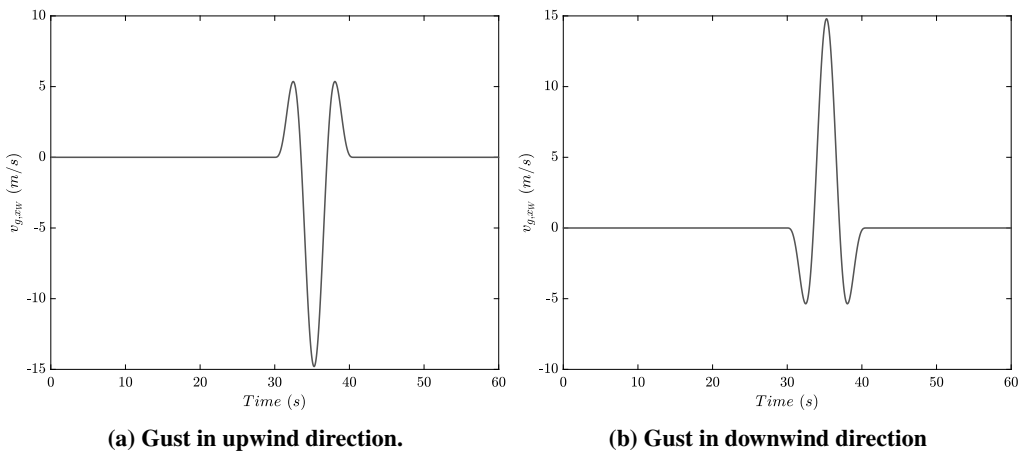


Fig. 16 Mexican hat wind gusts in up- and downwind direction.

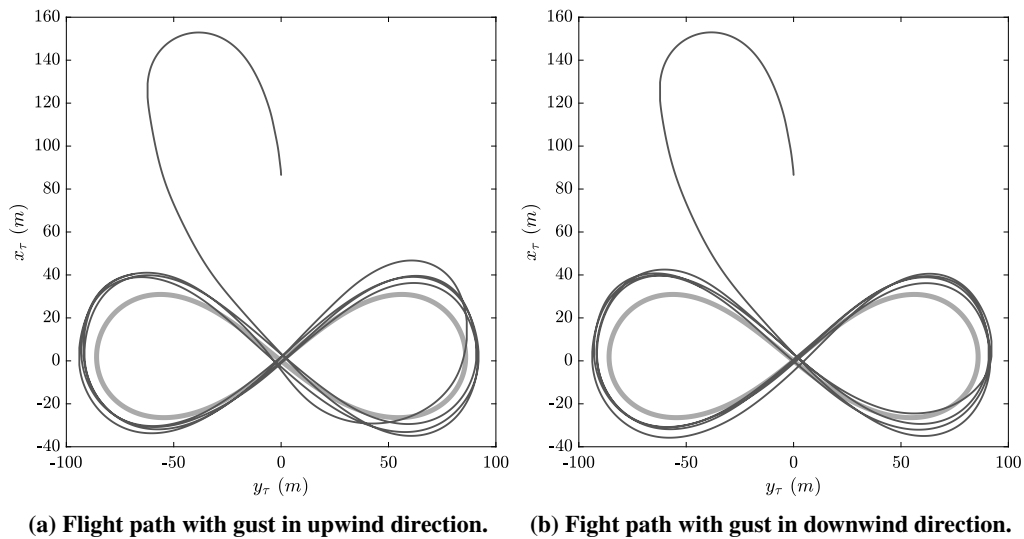


Fig. 17 View of the flight paths in mean path elevation angle direction.

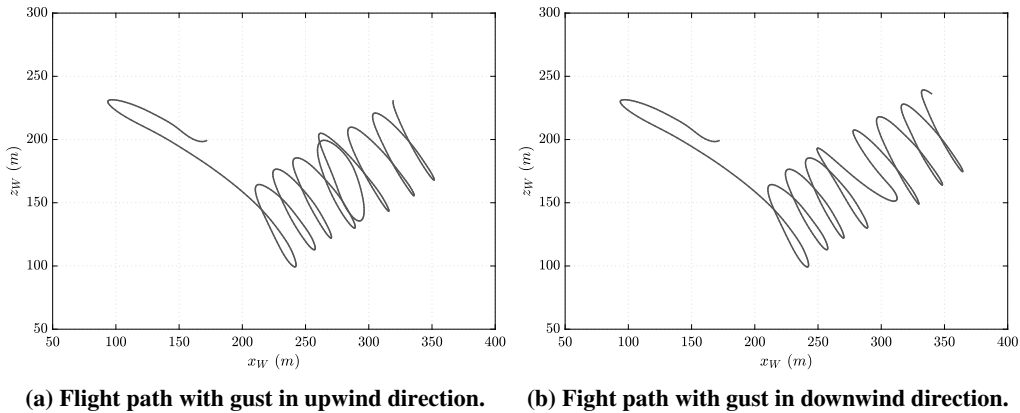


Fig. 18 Flight paths in x_W - z_W plane.

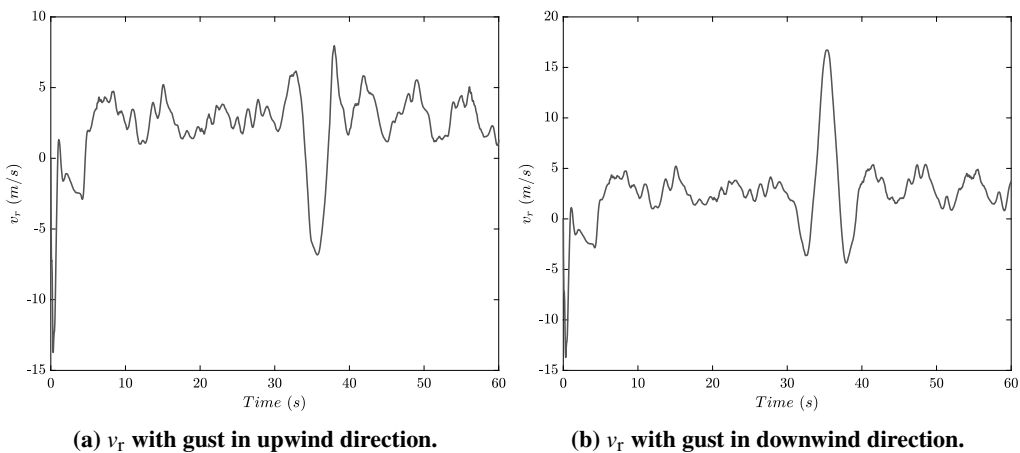


Fig. 19 Reeling out speed variations.

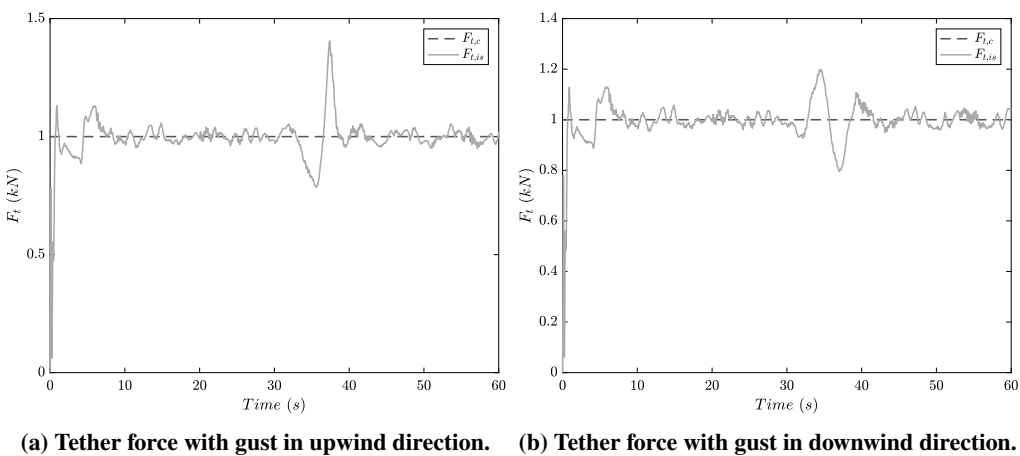


Fig. 20 Tether force variations.

automatically in case of angle of attack saturation. Challenging phases during the pumping cycle are the transitions from the traction to the retraction phase and vice versa. Due to the rapid tether force changes in these phases, overshoots in sideslip angle and angle of attack are present although these peaks occurred only for a short period of time and the resulting tracking errors could be regulated back to the set point by the respective feedback controller. The radial

direction control using the winch shows that the tether force set point can be tracked effectively by directly calculating a torque command as a function of the force tracking error. However, this leads to a high variance in the reeling speed and therefore to oscillations in the mechanical power output. This effect can be reduced by additionally using the pitch of the aircraft to control the airspeed. In return, this would lead to a less aggressive reeling speed adaption and hence a reduced variance of the mechanical power. The main task of the winch controller is to react to sudden wind speed changes, such as gusts, through adaption of the reeling out speed. The presented results demonstrate the effectiveness of this gust load alleviation strategy.

Acknowledgments

This research has been supported financially by the project AWESCO (H2020-ITN-642682), funded by the European Union's Horizon 2020 research and innovation program under the Marie Skłodowska-Curie grant agreement No. 642682.

References

- [1] Ahrens, U., Diehl, M., and Schmehl, R. (eds.), *Airborne Wind Energy*, Green Energy and Technology, Springer, Berlin Heidelberg, 2013. doi:10.1007/978-3-642-39965-7.
- [2] Schmehl, R. (ed.), *Airborne Wind Energy – Advances in Technology Development and Research*, Green Energy and Technology, Springer, Singapore, 2018. doi:10.1007/978-981-10-1947-0.
- [3] Cherubini, A., Papini, A., Vertechy, R., and Fontana, M., “Airborne Wind Energy Systems: A review of the technologies,” *Renewable and Sustainable Energy Reviews*, Vol. 51, 2015, pp. 1461–1476. doi:10.1016/j.rser.2015.07.053.
- [4] Fechner, U., and Schmehl, R., “Design of a Distributed Kite Power Control System,” *Proceedings of the 2012 IEEE International Conference on Control Applications*, IEEE, Dubrovnik, Croatia, 2012, pp. 800–805. doi:10.1109/CCA.2012.6402695.
- [5] Zraggen, A. U., Fagiano, L., and Morari, M., “On real-time optimization of airborne wind energy generators,” *Proceedings of the 52nd IEEE Conference on Decision and Control*, IEEE, Firenze, Italy, 2013, pp. 385–390. doi:10.1109/CDC.2013.6759912.
- [6] Erhard, M., and Strauch, H., “Flight control of tethered kites in autonomous pumping cycles for airborne wind energy,” *Control Engineering Practice*, Vol. 40, 2015, pp. 13–26. doi:10.1016/j.conengprac.2015.03.001.
- [7] Fagiano, L., Zraggen, A. U., Morari, M., and Khammash, M., “Automatic control of tethered wings for airborne wind energy: design and experimental results,” *Proceedings of the European Control Conference (ECC13)*, Zurich, Switzerland, 2013. doi:10.23919/ECC.2013.6669174.
- [8] Jehle, C., and Schmehl, R., “Applied Tracking Control for Kite Power Systems,” *AIAA Journal of Guidance, Control, and Dynamics*, Vol. 37, No. 4, 2014, pp. 1211–1222. doi:10.2514/1.62380.
- [9] Fagiano, L., Nguyen-Van, E., Rager, F., Schnez, S., and Ohler, C., “Automatic Take-Off of a Tethered Aircraft for Airborne Wind Energy: Control Design and Experimental Results,” *IFAC-Papers OnLine*, Vol. 50, No. 1, 2017, pp. 11932–11937. doi:10.1016/j.ifacol.2017.08.1456, 20th IFAC World Congress.
- [10] Johnson, E. N., “Limited Authority Adaptive Flight Control,” Ph.D. thesis, Georgia Institute of Technology, 2000. URL <http://hdl.handle.net/1853/12953>.
- [11] Ilzhöfer, A., Houska, B., and Diehl, M., “Nonlinear MPC of kites under varying wind conditions for a new class of large-scale wind power generators,” *International Journal of Robust and Nonlinear Control*, Vol. 17, No. 17, 2007, pp. 1590–1599. doi:10.1002/rnc.1210.
- [12] Stevens, B. L., Lewis, F. L., and Johnson, E. N., *Aircraft control and simulation*, 3rd ed., John Wiley & Sons Inc., Hoboken, New Jersey, 2016. doi:10.1002/9781119174882.
- [13] Beard, R. W., and McLain, T. W., *Small Unmanned Aircraft: Theory and Practice*, Princeton University Press, Princeton, NJ, USA, 2012.
- [14] Brockhaus, R., Alles, W., and Luckner, R., *Flugregelung*, Springer-Verlag, Berlin Heidelberg, 2011. doi:10.1007/978-3-642-01443-7.

- [15] Wang, J., “Novel Control Approaches to Quadrotors Inspired by Dynamic Inversion and Backstepping,” Ph.D. thesis, Technical University of Munich, 2015. URL <https://d-nb.info/107900176X/34>.
- [16] Fechner, U., van der Vlugt, R., Schreuder, E., and Schmehl, R., “Dynamic Model of a Pumping Kite Power System,” *Renewable Energy*, Vol. 83, 2015, pp. 705–716. doi:10.1016/j.renene.2015.04.028.
- [17] Calaf, M., Meneveau, C., and Meyers, J., “Large eddy simulation study of fully developed wind-turbine array boundary layers,” *Physics of Fluids*, Vol. 22, No. 1, 2010, p. 015110. doi:10.1063/1.3291077.
- [18] Goit, J., and Meyers, J., “Optimal control of energy extraction in wind-farm boundary layers,” *Journal of Fluid Mechanics*, Vol. 768, 2015, pp. 5–50.
- [19] Munters, W., Meneveau, C., and Meyers, J., “Turbulent inflow precursor method with time-varying directions for large-eddy simulations and applications to wind farms,” *Boundary-Layer Meteorology*, Vol. 159, 2016, pp. 305–328.
- [20] Rapp, S., and Schmehl, R., “Vertical Takeoff and Landing of Flexible Wing Kite Power Systems,” *AIAA Journal of Guidance, Control, and Dynamics*, Vol. 41, No. 11, 2018, pp. 2386–2400. doi:10.2514/1.G003535.
- [21] Fagiano, L., Zraggen, A. U., Morari, M., and Khammash, M., “On control of tethered wings for airborne wind energy,” *Proceedings of the 2013 American Control Conference*, IEEE, Washington, DC, USA, 2013.
- [22] Zraggen, A. U., “Automatic Power Cycles for Airborne Wind Energy Generators,” Ph.D. thesis, ETH Zurich, 2014. doi:10.3929/ethz-a-010350742.
- [23] Fechner, U., and Schmehl, R., “Flight Path Control of Kite Power Systems in a Turbulent Wind Environment,” *Proceedings of the 2016 American Control Conference (ACC)*, IEEE, Boston, MA, USA, 2016, pp. 4083–4088. doi:10.1109/ACC.2016.7525563.
- [24] Erhard, M., and Strauch, H., “Theory and Experimental Validation of a Simple Comprehensible Model of Tethered Kite Dynamics Used for Controller Design,” *Airborne Wind Energy*, edited by U. Ahrens, M. Diehl, and R. Schmehl, Green Energy and Technology, Springer, Berlin Heidelberg, 2013, Chap. 8, pp. 141–165. doi:10.1007/978-3-642-39965-7_8.
- [25] Booth, J., *A Treatise on Some New Geometrical Methods: The geometrical properties of elliptic integrals, rotatory motion, the higher geometry, and conics derived from the cone, with an appendix to the first volume*, A Treatise on Some New Geometrical Methods, Longmans, Green, Reader, and Dyer, 1873.
- [26] Holzapfel, F., and Sachs, G., “Dynamic Inversion Based Control Concept with Application to an Unmanned Aerial Vehicle,” AIAA Guidance, Navigation, and Control Conference and Exhibit, Providence, Rhode Island, 2004. doi:10.2514/6.2004-4907.
- [27] Åström, K. J., and Hägglund, T., *Advanced PID Control*, ISA – The Instrumentation, Systems and Automation Society, 2006.
- [28] Karlsson, E., Schatz, S. P., Baier, T., Dörhöfer, C., Gabrys, A., Hochstrasser, M., Krause, C., Lauffs, P. J., Mumm, N. C., Nürnberger, K., Peter, L., Schneider, V., Spiegel, P., Steinert, L., Zollitsch, A. W., and Holzapfel, F., “Automatic flight path control of an experimental DA42 general aviation aircraft,” *2016 14th International Conference on Control, Automation, Robotics and Vision (ICARCV)*, 2016, pp. 1–6. doi:10.1109/ICARCV.2016.7838566.
- [29] Bacon, B. J., Ostroff, A. J., and Joshi, S. M., “Reconfigurable NDI controller using inertial sensor failure detection and isolation,” *IEEE Transactions on Aerospace and Electronic Systems*, Vol. 37, No. 4, 2001, pp. 1373–1383. doi:10.1109/7.976972.
- [30] Lu, P., van Kampen, E.-J., de Visser, C., and Chu, Q., “Aircraft fault-tolerant trajectory control using Incremental Nonlinear Dynamic Inversion,” *Control Engineering Practice*, Vol. 57, 2016, pp. 126–141. doi:10.1016/j.conengprac.2016.09.010.
- [31] Schreuder, E. N. J., “Improving winch control performance in Kite Power Systems using gain scheduling and a compliant element,” Master of science thesis, Delft University of Technology, 2013.
- [32] Föllinger, O., *Regelungstechnik*, 12th ed., VDE Verlag GmbH, Berlin, Germany, 2016.
- [33] Lavretsky, E., and Wise, K. A., *Robust and adaptive control*, Springer-Verlag London, 2013. doi:10.1007/978-1-4471-4396-3.
- [34] “IEC 61400-1 Wind turbines - Part 1: Design requirements,” Tech. rep., Geneva, Switzerland: International Electrotechnical Commission, 2005.